from hPSCs. We found that the HBCs derived from hPSCs can be maintained and proliferated on human laminin-111 (LN111)-coated dishes. To demonstrate that expandable, multipotent, and safe (i.e., devoid of residual undifferentiated cells) hPSC-derived HBCs could be maintained under our culture condition, the hPSC-derived HBCs were used for hepatic and biliary differentiation, colony assay, and transplantation into immunodeficient mice.

RESULTS

Human PSC-Derived Hepatoblast-like Cells Could Adhere onto Human LN111 via Integrin α6 and β1

The HBCs were generated from hPSCs (hESCs and hiPSCs) as described in Figure 1A (details of the characterization of hPSC-derived HBCs are described in Figure 3). Definitive endoderm differentiation of hPSCs was promoted by stage-specific transient transduction of FOXA2 in addition to the treatment with appropriate soluble factors (such as Activin A). Overexpression of FOXA2 is not necessary for establishing the hPSC-derived HBCs, but it is helpful for efficient generation of the hPSC-derived HBCs. On day 9, these hESC-derived populations contained two cell populations with distinct morphology (Figure 1B). One population resembled human hepatic stem cells that were isolated from human fetal liver (shown in red) (Schmelzer et al., 2007), whereas the other population resembled definitive endoderm cells (shown in green) (Hay et al., 2008). The population that resembled human hepatic stem cells was alpha-1-fetoprotein (AFP) positive, whereas the other population was AFP negative (Figure 1C, left). On day 9, the percentage of AFP-positive cells was approximately 80% (Figure 1C, right). To characterize these two cell populations (hESC-derived HBC and non-HBC [NHBC] populations), the colonies were manually isolated by using a pipette, and then the gene expression analysis was performed. The gene expression levels of *AFP*, *CD133*, *EpCAM*, *CK8*, and *CK18* in the hESC-derived HBCs were higher than those in the bulk population containing both hESC-derived HBCs and NHBCs (*CD133*, *EpCAM*, *CK8*, and *CK18* were named as pan-hepatoblast markers and are known to be strongly expressed in both human hepatic stem cells and hepatoblasts [Schmelzer et al., 2007; Zhang et al., 2008]) (Figure 1D). On the other hand, the gene expressions of *AFP*, *CD133*, *EpCAM*, *CK8*, and *CK18* in the hESC-derived NHBCs were hardly detected. The gene expression levels of DE, mesendoderm, and pluripotent markers in the hESC-derived NHBCs were higher than those in the hESC-derived HBCs, indicating that the hESC-derived NHBCs could remain in a more undifferentiated state than the hESC-derived HBCs (Figures S1A–S1C available online). These results suggest that hepatoblast-like cells could be differentiated from hPSCs.

To purify the hESC-derived HBCs, these cells were plated onto dishes coated with various laminins. There are 15 different laminin isoforms in human tissues. Although laminin is known to be useful to sustain mouse hepatoblasts (Tanimizu et al., 2004), it remains unknown which human laminin isoform has the potential to purify and expand the HBCs. To identify a human laminin isoform that would be useful for purifying hESC-HBCs, the hESC-HBCs and -NHBCs were plated onto dishes coated with various types of commercially available human laminins (Figure 1E). The hESC-derived HBCs could more efficiently adhere onto the human LN111-coated dish compared with hESC-derived NHBCs or unseparated populations (containing both HBCs and NBCs). These data suggest that a hESC-derived HBC population can be purified from the unseparated populations by culturing on human LN111-coated dishes. Because integrins are known to be important molecules for cell adhesion to the ECM including laminins, we expected that certain types of integrins would allow selective adhesion of the hESC-derived HBCs to human LN111-coated dish. The gene expression levels of various integrins were examined (Figure 1F). Among the integrin α subunits, the gene expression level of *integrin α6* in the hESC-derived HBCs was significantly higher than that in the hESC-derived NHBCs. In contrast, among the integrin β subunits, the gene expression level of *integrin β1* was higher than those of *integrin β2* and *β3* in all cell populations. The hESC-derived HBCs, but not NHBCs, expressed both integrin α6 and β1 (Figure S1D). Almost all adhesion of the hESC-derived HBCs to a human LN111-coated dish was inhibited by both function-blocking antibodies to integrin α6 and β1 (Figure 1G). These results indicated that the hESC-derived HBCs could attach to a human LN111-coated dish via integrin α6 and β1.

The hPSC-Derived HBCs Could Be Proliferated and Maintained on a Human LN111-Coated Dish

To obtain the purified hESC-derived HBC population, the hESC-derived cells (day 9) were plated onto a human LN111-coated dish, and then unattached cells were removed at 15 min after plating (Figure 2A). Among various laminins, only human LN111 could proliferate (Figure 2B) and purify (Figure 2C) the AFP-positive population in the presence of HGF and EGF. During culture on the human LN111-coated dish, the morphology of the hESC-derived HBCs gradually changed into that of human hepatoblasts (Figure S1E) (Schmelzer et al., 2007). Therefore, the characteristics of hESC-derived HBCs might be changed by culturing on a human LN111-coated dish (details of the characterization of the hESC-derived HBCs are described in Figure 3). After culturing on a human LN111-coated

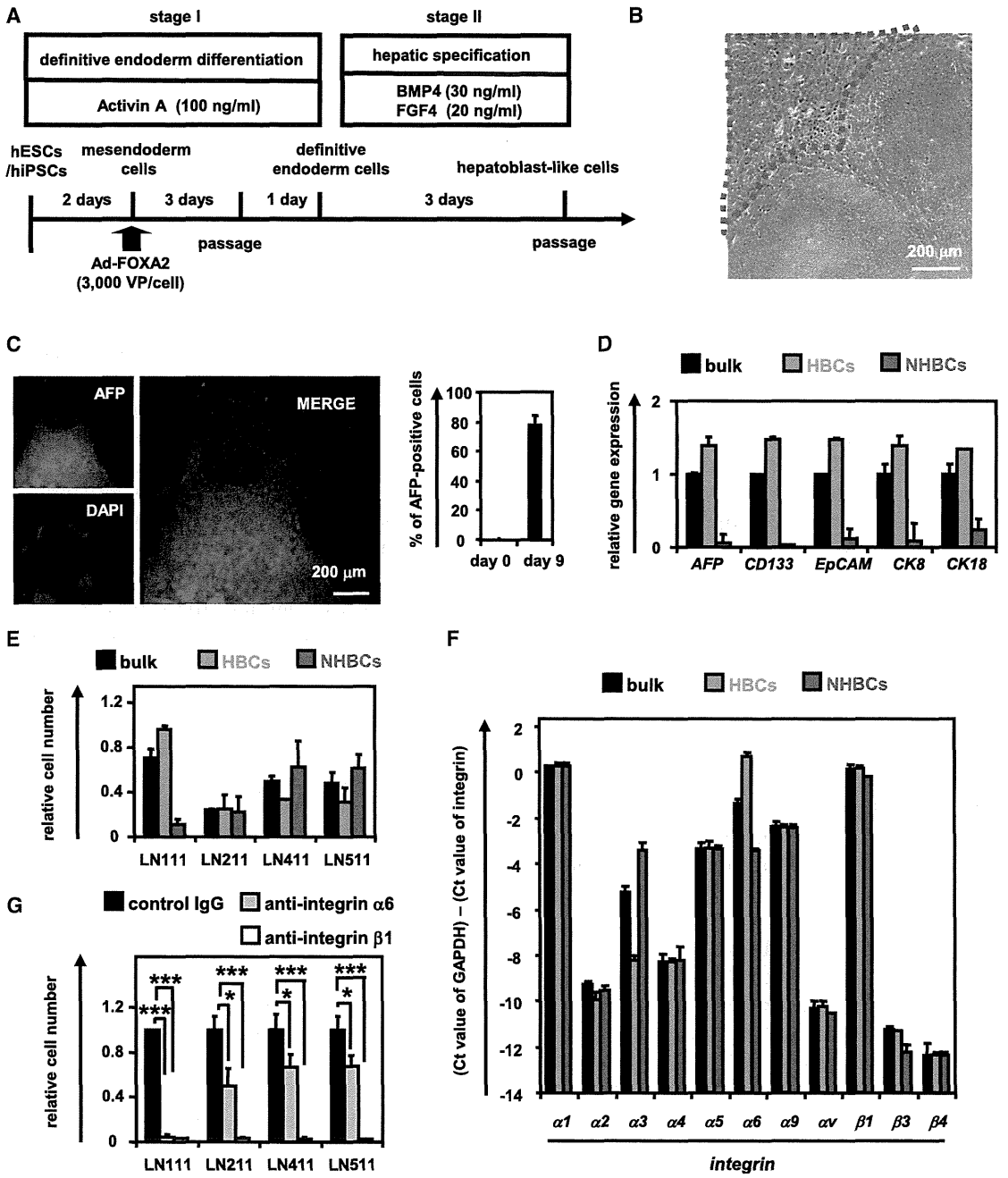

Figure 1. The Human ESC-Derived HBCs Selectively Attached to a Human LN111-Coated Dish via Integrin α6 and β1

(A) The procedure for the differentiation of hESCs (H9) into hepatoblast-like cells (HBCs) is presented schematically. Details are described in the Experimental Procedures.

(B) Phase-contrast micrographs of the hESC-derived HBCs (red) and non-HBCs (NHBCs) (green) are shown.

(C) The hESC-derived cells (day 9) were subjected to immunostaining with anti-AFP (red) antibodies. The percentage of AFP-positive cells was examined on day 0 or 9 by using FACS analysis. Data represent the mean ± SD from ten independent experiments. Cells on "day 0" and "day 9" were compared using Student's t test ($p < 0.01$).

(D) On day 9, the hESC-derived HBCs and NHBCs were manually picked, and the gene expression levels of *AFP* and pan-hepatoblast markers (*CD133*, *EpCAM*, *CK8*, and *CK18*) were measured by real-time RT-PCR. The gene expression levels of *AFP* and pan-hepatoblast markers in the hESC-derived cells (day 9; bulk) were taken as 1.0. Data represent the mean ± SD from four independent experiments. The gene expression levels in the HBCs were significantly different among the three groups (bulk, HBCs, and NHBCs) based on analysis with one-way ANOVA followed by Bonferroni post hoc tests ($p < 0.05$).

(legend continued on next page)

dish for a week, almost all of the cells were still AFP positive (Figures 2C and 2D). To characterize the cells cultured on various types of human laminins for 7 days, the gene expression levels of *AFP* and pan-hepatoblast (*CD133*, *CK8*, *CK18*, and *EpCAM*) markers were examined on day 16 (Figure 2E). The gene expression levels of *AFP* and pan-hepatoblast markers in the hESC-derived HBCs P1 (HBCs passaged once) did not change as compared with those of the hESC-derived HBCs (day 9; HBC P0) (the definitions of HBC P0, P1, P10, and clone in the present study are shown in Figure S3). The gene expression levels of mature hepatocyte and cholangiocyte markers in the hESC-derived HBC P1 did not change as compared with those of the hESC-derived HBC P0 (day 9) (Figure S1F). These results suggest that the characteristics of the hESC-derived HBC P1 are similar to those of the hESC-derived HBC P0, although their morphologies are quite different from each other. Interestingly, the gene expression levels of mature cholangiocyte markers in the cells cultured on human LN411- or 511-coated dishes were upregulated as compared with those of the hESC-derived HBC P0 (day 9) (Figure S1F), suggesting that human LN411 and 511 might promote biliary differentiation. Importantly, both hESC-derived HBCs and hiPSC-derived HBCs could extensively proliferate on a human LN111-coated dish for more than 15 passages (Figure 2F) in the presence of HGF and EGF. Doubling times of hESC (H9)-derived HBCs and hiPSC (Dotcom)-derived HBCs were approximately 78 and 67 hr, respectively. Almost all of the populations cultured on a human LN111-coated dish were AFP positive (Figure 2G). Taken together, these results suggested that the hPSC-derived HBCs would proliferate and be maintained on a human LN111-coated dish.

Characterization of the hESC-Derived HBCs

To characterize the hESC-derived HBCs, the gene expression profiles in the hESC-derived purified HBCs (HBC P0), short-term cultured HBCs (HBCs passaged once [HBC P1]), and long-term cultured HBC (HBCs passaged ten times [HBC P10]) were examined. The hESC-derived HBCs were AFP positive (Figure 3A). Although the hESC-derived HBC P0 were negative for ALB, CK7, and CK19, the hESC-derived HBC P1 and P10 were positive for these genes (Figure 3A). Both integrin α6 and β1 (receptors of LN111) were strongly expressed in the hESC-derived HBC P0, P1, and P10 (Figure 3B). The gene expression levels of human hepatic stem cell markers (*N-CAM* and *Claudin 3* [Schmelzer et al., 2007]; these are not expressed in human hepatoblasts) in the hESC-derived HBC P0 were higher than those of the hESC-derived HBC P1 and P10 (Figure 3C). However, the gene expression level of *CK19* in the hESC-derived HBC P0 was lower than that of the hESC-derived HBC P1 and P10. The gene expression levels of pan-hepatoblast markers in the hESC-derived HBC P0 were similar to those of the hESC-derived HBC P1 and P10 (Figure 3D). The gene expression levels of human hepatoblast markers (*ALB*, *CYP3A7*, and *I-CAM* (Schmelzer et al., 2007), none of which were expressed in human hepatic stem cells) in the hESC-derived HBC P1 and P10 were higher than those of the hESC-derived HBC P0 (Figure 3E). However, the AFP expression level in the hESC-derived HBC P0 was similar to that of the hESC-derived HBC P1 and P10. Because the gene expression levels of mature hepatocyte and cholangiocyte markers in the hESC-derived HBC P1 and P10 were not increased as compared with those in the hESC-derived HBC P0 (Figure 3F), the hESC-derived HBC P1 and P10 were not segregated into either of the hepatic and biliary lineages. We also examined the gene expression levels of hepatoblast markers, which have been reported only in mice and not in humans (Figure 3G). The characteristics of the hPSC-derived HBCs are summarized in Figure S3. In addition, hESC-derived HBC P0 and HBC P10 showed normal karyotypes (Figure S2A). Therefore, the genetic stability of the HBCs was confirmed throughout the maintenance period. Taken together, these results suggest that the hESC-derived HBC P0 resemble human hepatic stem cells and the hESC-derived HBC P1 and P10 resemble human hepatoblasts, although some gene expression patterns in the hESC-derived HBCs differ from those in human hepatic stem cells and human hepatoblasts, respectively.

(E) The hESC-derived cells (day 9; bulk), HBCs, and NHBCs were plated onto human LN111-, 211-, 411-, or 511-coated dishes, and the attached cells were counted at 60 min after plating. The cell number that was initially plated was taken as 1.0. Data represent the mean ± SD from four independent experiments. The number of attached HBCs on LN111-coated dishes were significantly different among three groups (bulk, HBCs, and NHBCs) based on analysis with one-way ANOVA followed by Bonferroni post hoc tests ($p < 0.05$).

(F) The gene expression levels of the indicated integrins were measured in the hESC-derived cells (day 9; bulk), HBCs, and NHBCs by real-time RT-PCR. Data represent the mean ± SD from four independent experiments. The gene expression levels of *integrin α3* and *α6* in the HBCs were significantly different among three groups (bulk, HBCs, and NHBCs) based on analysis with one-way ANOVA followed by Bonferroni post hoc tests ($p < 0.05$).

(G) The adhesion of the hESC-derived HBCs to human LN111-, 211-, 411-, or 511-coated dishes was examined by using the indicated integrin antibodies. IgG antibodies were used as a control for uninhibited cell adhesion. The number of attached cells was estimated at 60 min after plating. The cell number in the control IgG-treated group was taken as 1.0. Data represent the mean ± SD from three independent experiments. "Control IgG" and "anti-integrin α6 or integrin β1" were compared using Student's t test. *$p < 0.05$; ***$p < 0.001$. See also Figure S1 and Tables S2–S5.

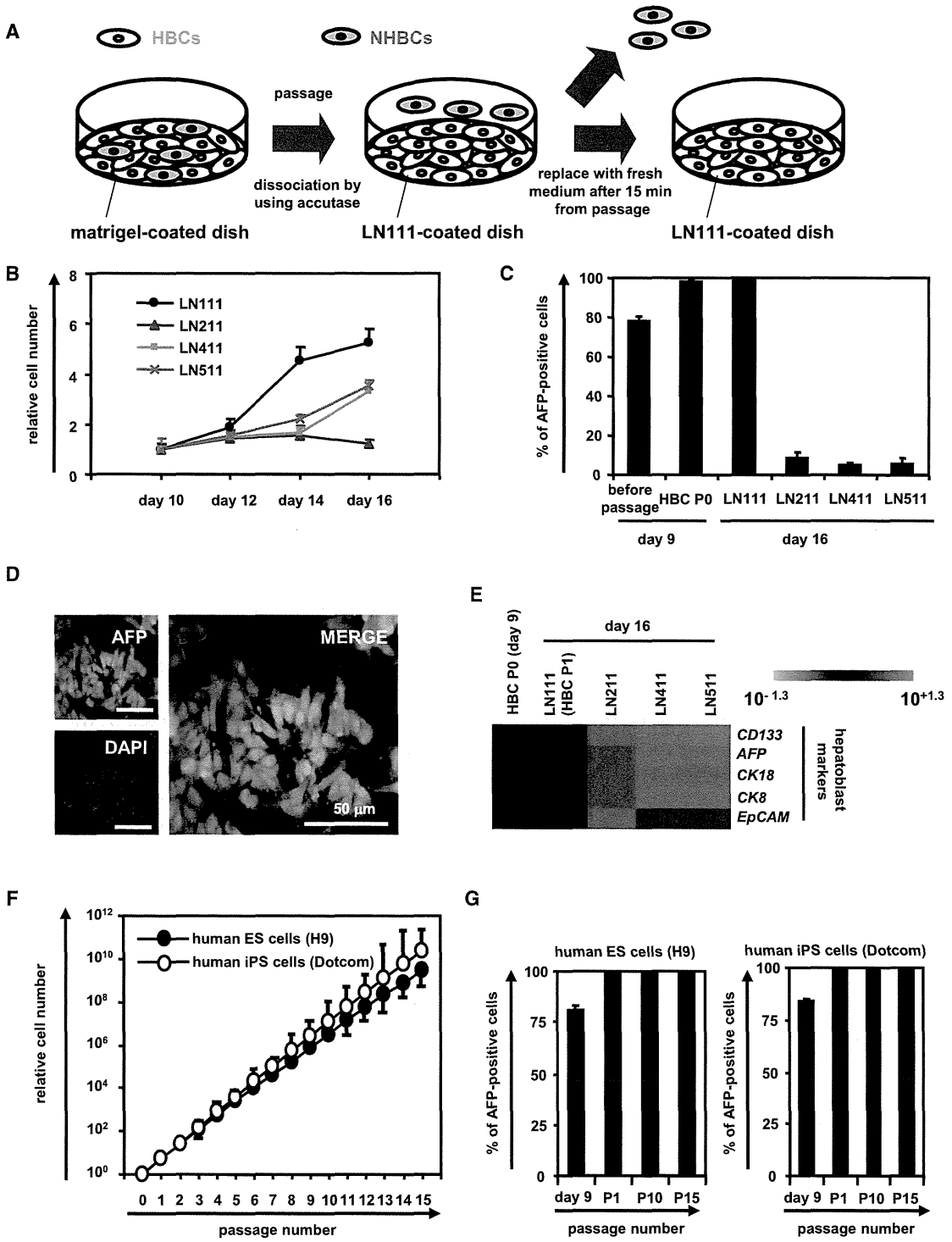

Figure 2. The hESC-Derived HBCs Could Be Proliferated and Maintained on a Human LN111-Coated Dish

(A) The hESC (H9)-derived cells (day 9) were plated onto a human LN111-coated dish. At 15 min after plating, the unattached cells were removed.

(B) The hESC (H9)-derived cells (day 9) were plated onto a human LN111, 211, 411, or 511-coated dish, and then the cell number were counted on days 10, 12, 14, and 16. The cell number on day 10 was taken as 1.0. Data represent the mean ± SD from three independent experiments. "LN111" was significantly different among four groups (LN111, 211, 411, and 511) on day 14 and 16 based on analysis with one-way ANOVA followed by Bonferroni post hoc tests ($p < 0.05$).

(legend continued on next page)

In order to examine whether the hESC-derived HBC P0 have the potential to proliferate clonally on various types of human laminins, single HBCs were plated on separate wells of a human LN111-coated 96-well plate at a low density (one cell per one well) (Table S1). Single cells that attached to the human LN111-coated dish were AFP positive and HNF4α positive (Figure S2B). At 7 days after plating, the hESC-derived HBC colonies (albumin [ALB]- and cytokeratin 7 [CK7] double positive) (a representative colony is shown in Figure S2C) were efficiently generated from the hESC-derived HBC P0 on a LN111-coated dish. Taken together, these results showed that the hESC-derived HBCs could be generated from both the hESC-derived HBC P0 population and the single hESC-derived HBC P0.

The hPSC-Derived HBCs Could Differentiate into Both Hepatic and Biliary Lineages In Vitro

To examine whether the hESC-derived HBCs have the potential to differentiate into both hepatic and biliary lineages, first, these cells were differentiated into hepatocyte-like cells as described in Figure 4A. After 2 weeks of hepatic differentiation, almost all of the cells were polygonal in shape (Figure 4B) and were CYP3A4, αAT, and ALB positive (Figure 4C). The gene expression levels of mature hepatocyte markers in the HBC P0-, HBC P10-, or HBC clone-derived hepatocyte-like cells were higher than those in the cells that had not undergone hepatic differentiation (Figure 4D), although the gene expression levels of mature cholangiocyte markers in these cells did not change (Figure 4E). The ASGR1-positive cells in the HBC P0-, HBC P10-, and HBC clone-derived population accounted for approximately 60%, 90%, and 90% of the total, respectively (Figure 4F). The HBC P0-, HBC P10-, or HBC clone-derived hepatocyte-like cells had the ability to produce ALB (Figure 4G, left) and urea (Figure 4G, right). Next, the hESC-derived HBCs were differentiated into cholangiocyte-like cells as described in Figure 4H. After 2 weeks of biliary differentiation, tubular structures (Figure 4I) that were CK7 positive (Figure 4J) were observed. Although the gene expression levels of mature hepatocyte markers (Figure 4K) in the HBC P0-, HBC P10-, or HBC clone-derived cholangiocyte-like cells did not change, the gene expression levels of mature cholangiocyte markers (Figure 4L) in these cells were higher than those in the cells that had not undergone differentiation. Similar results were obtained by using another hESC line (H1) and hiPSC line (Dotcom) (Figure S4). Moreover, HBC-derived hepatocyte-like cells exhibited CYP metabolism capacity (Figure S5A) and a functional urea cycle that could response to ammonia (Figure S5B) and were considered to have potential to be applied in the prediction of drug-induced hepatotoxicity (Figure S5C). Taken together, these results indicated that the hPSC-derived HBCs have the ability to differentiate into both hepatic and biliary lineages in vitro.

In Vivo Cell Transplantation Assays of the hPSC-Derived HBCs

To examine whether the hESC-derived HBCs could be used for hepatocyte transplantation, these cells were transplanted into CCl_4-treated immunodeficient mice as shown in Figure 5A. The hepatocyte functionality of the hESC-derived HBC P0 or HBC P10 was assessed by measuring secreted human ALB levels in the recipient mice (Figure 5B). Although human ALB was detected in the mice that were transplanted with the hESC-derived HBC P0 or HBC P10, it was not detected in the mice that were not transplanted with these cells. The ALB-positive cells were observed in mice transplanted with the hESC-derived HBC P0 or HBC P10 (Figure 5C). Most of the ALB-positive cells in mice transplanted with the hESC-derived HBC P10 were AFP negative (Figure 5D), indicating that transplanted hESC-derived HBCs were differentiated into mature hepatocyte-like cells (some of them were binuclear [Figure 5E, white arrows]). These results demonstrated that hESC-derived HBCs have the potential to be applied for hepatocyte transplantation.

(C) The hESC-derived cells (day 9) were plated onto a human LN111, 211, 411, or 511-coated dish. The percentage of AFP-positive cells was examined by using FACS analysis on day 9 (before passage and after passage [HBC P0]) or day 16. Data represent the mean ± SD from three independent experiments.

(D) The hESC-derived cells cultured on a human LN111-coated dish for 7 days were subjected to immunostaining with anti-AFP (green) antibodies.

(E) The hESC-derived cells (day 9) were plated onto human LN111, 211, 411, or 511-coated dishes. The gene expression levels of *AFP* and pan-hepatoblast markers (*CD133*, *EpCAM*, *CK8*, and, *CK18*) were measured by real-time RT-PCR on day 16. The gene expression levels in the hESC-derived HBCs (the LN111-attached cells were collected at 15 min after plating) were taken as 1.0.

(F) The HBCs derived from hESCs (H9) or hiPSCs (Dotcom) were cultured and cell growth was analyzed by obtaining a cell count at each passage. Data represent the mean ± SD from three independent experiments.

(G) The percentage of AFP-positive cells was examined by using FACS analysis on day 9 (before passage), P1 (HBCs passaged once), P10 (HBCs passaged ten times), and P15 (HBCs passaged 15 times). Data represent the mean ± SD from seven independent experiments.

See also Tables S2 and S3.

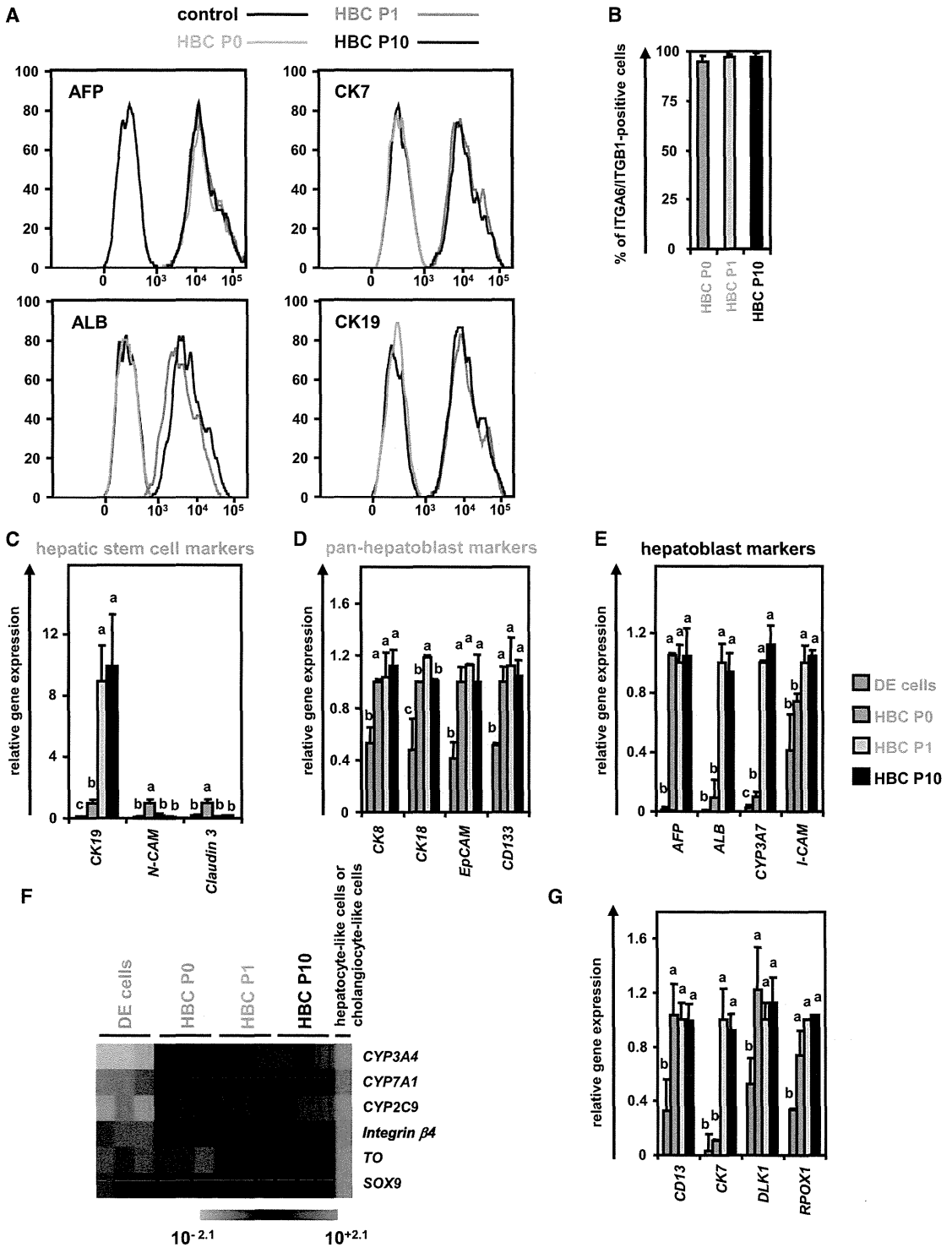

Figure 3. The hESC-Derived HBCs Were Characterized

(A and B) The hESCs (H9) were differentiated according to Figure 1A and then passaged onto a human LN111-coated dish. The attached cells (hESC-derived HBCs [HBC P0]) were collected at 15 min after plating. The percentage of AFP-positive, ALB-positive, CK7-positive, CK19-positive (A), and integrin α6- and integrin β1-double positive (B) cells in the hESC-derived HBC P0, HBC P1 (HBCs passaged once), and HBC P10 (HBCs passaged ten times) populations was estimated by using FACS analysis. Data represent the mean ± SD from seven independent experiments.

(legend continued on next page)

DISCUSSION

The main purpose of this study was to establish and characterize expandable HBCs from hPSCs. First, we identified that human LN111 could support self-renewal and proliferation of hPSC-derived HBCs in the presence of HGF and EGF. Second, we showed that the hPSC-derived HBCs have the potential to segregate into both hepatic and biliary lineages, and to integrate into the mouse liver parenchyma.

We have demonstrated that the hPSC-derived HBCs could be maintained on a human LN111-coated dish in an integrin α6- and β1-dependent manner (Figure 1). It is known that undifferentiated hPSCs could be maintained on a human LN511-coated dish but not on a human LN111-coated dish (Rodin et al., 2010). This might suggest that human LN111 has the potential not only to selectively maintain HBCs, but also to eliminate residual undifferentiated cells. Our hepatoblast-like cells could efficiently proliferate for more than 3 months on a human LN111-coated dish (Figure 2). In the human liver development (during 5–10 weeks gestation), laminin is observed in both the perisinusoidal space and portal tracts (Couvelard et al., 1998). The expression of laminin is localized around the periportal biliary trees during the later stage of liver development (Couvelard et al., 1998). Hepatic stem cells reside around the hepatic portal area (Clément et al., 1988). It is also known that laminin is accumulated around oval cells although laminin is not expressed around quiescent mature hepatocytes (Paku et al., 2001). These facts suggest that laminin plays an important role in the maintenance and proliferation of hepatoblasts.

The hPSC-derived HBC P10 and clone were positive for hepatoblast markers (AFP, ALB, CYP3A7, and I-CAM), but negative for hepatic stem cell markers (N-CAM and Claudin 3) (Figure 3) (Schmelzer et al., 2007). Although the hPSC-derived HBCs were able to expand on human LN111-coated dish, Schmelzer et al. showed that human hepatoblasts do not proliferate under a monolayer culture condition, but human hepatic stem cells could self-replicate for more than 6 months (Schmelzer et al., 2007). Although further investigations of the hepatoblast characteristics in the hPSC-derived HBCs will be needed in the future, the results in the present study suggest that the characteristics of hPSC-derived HBCs expanded on human LN111-coated dishes were similar to those in human hepatoblasts isolated from the human liver (Schmelzer et al., 2007; Zhang et al., 2008).

The hPSC-derived HBCs had the ability to integrate into the mouse liver parenchyma (Figure 5), in the manner of human hepatic stem cells or hepatoblasts (Schmelzer et al., 2007). The human ALB serum levels (approximately 20–70 ng/ml) in mice transplanted with the hESC-derived HBC P0 or HBC P10 were comparable to those in the previous paper in which the hESC-derived definitive endoderm cells, hepatoblasts, and hepatocyte-like cells were transplanted into mice (Liu et al., 2011), but were lower than those of human liver chimeric mice (Tateno et al., 2004). Human ALB serum levels would increase if more suitable host mice, such as urokinase plasminogen activator-SCID mice were used (Tateno et al., 2004).

In this study, we have developed a technology for the maintenance and proliferation of hPSC-derived HBCs by using human LN111. To transplant these cells for purposes of regenerative medicine, a xeno-free culture condition for hPSC-derived HBCs must be developed in the future. It is hoped that the hPSC-derived HBCs and their derivatives will be helpful in various medical applications, such as drug screening and regenerative medicine.

EXPERIMENTAL PROCEDURES

hESC and hiPSC Culture

The hESC lines (H1 [WA01] and H9 [WA09] [WiCell Research Institute]) and the hiPSC line, Dotcom (JCRB number: JCRB1327) (Makino et al., 2009; Nagata et al., 2009), were maintained on a feeder layer of mitomycin-C-treated mouse embryonic fibroblasts (Millipore) with ReproStem medium (ReproCELL) supplemented with 5 and 10 ng/ml fibroblast growth factor 2 (FGF2) (Katayama Kagaku Kogyo), respectively. H1 and H9 were used following the Guidelines for Derivation and Utilization of Human Embryonic Stem Cells of the Ministry of Education, Culture, Sports, Science and Technology of Japan, and, furthermore, the study was approved by an independent ethics committee.

In Vitro Hepatoblast Differentiation

The differentiation protocol for the induction of definitive endoderm cells and hepatoblasts was based on our previous report with some modifications (Inamura et al., 2011; Takayama et al., 2012a, 2012b, 2013). In mesendoderm differentiation, hESCs/iPSCs were

(C–F) The gene expression levels of hepatic stem cell markers (C), pan-hepatoblast markers (D), hepatoblast markers (E), and mature hepatocyte (*CYP3A4*, *7A1*, *2C9*, and *TO*) or cholangiocyte markers (*integrin β4* and *SOX9*) (F) were measured in the definitive endoderm cells, HBC P0, HBC P1, or HBC P10 by real-time RT-PCR.

(G) The gene expression levels of *CD13*, *CK7*, *DLK1*, and *PROX1* were measured in the hESC-derived definitive endoderm cells, HBC P0, HBC P1, or HBC P10 by real-time RT-PCR. Data represent the mean ± SD from three independent experiments. Statistical significance was evaluated by ANOVA followed by Bonferroni post hoc tests to compare four groups (DE cells, HBC P0, HBC P1, and HBC P10). Groups that do not share the same letter are significantly different from each other ($p < 0.05$). DE, definitive endoderm cells.

See also Figures S2 and S3 and Tables S2–S4.

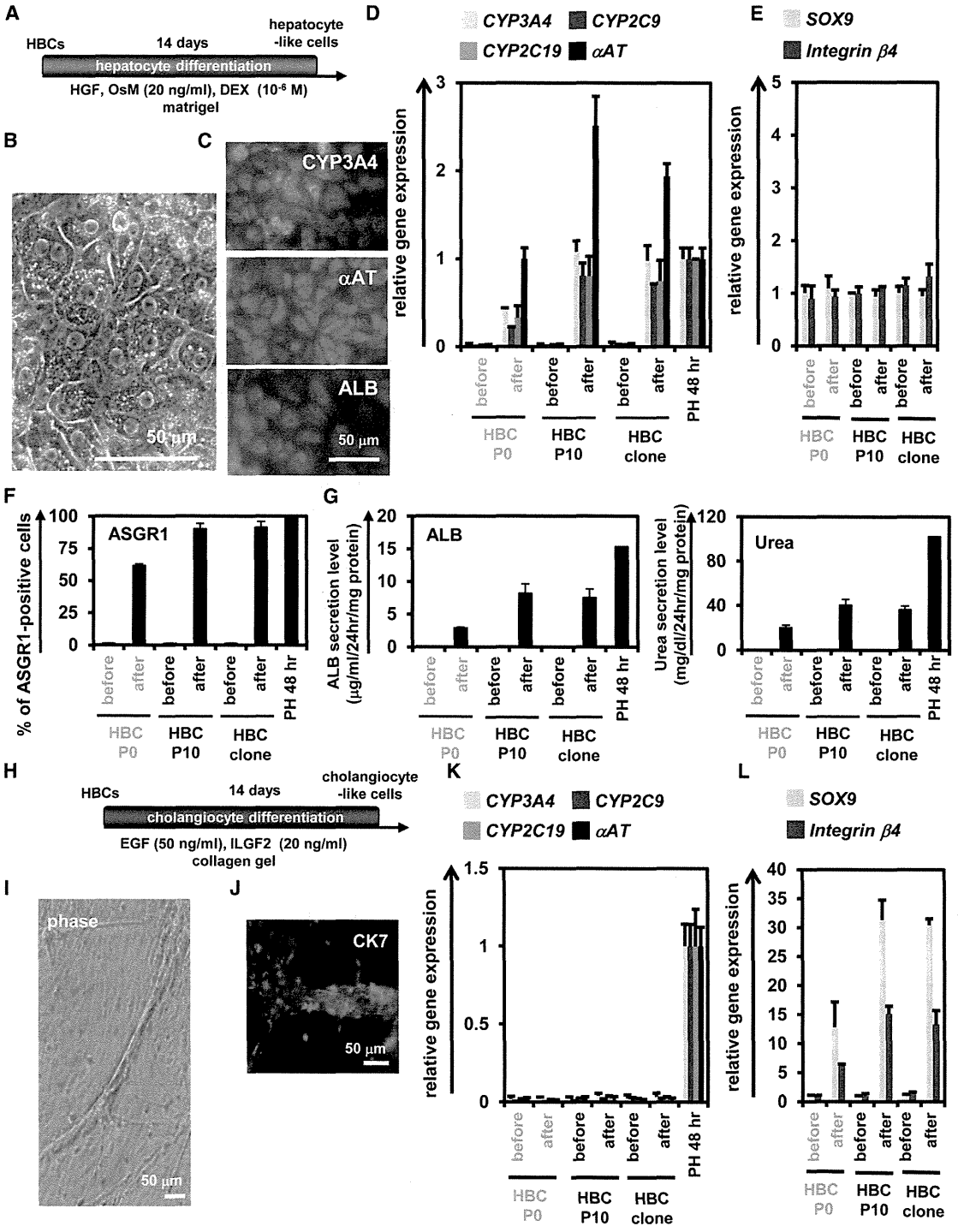

Figure 4. The hESC-Derived HBCs Could Differentiate into Both Hepatic and Biliary Lineages

(A) The procedure for differentiation of the hESC (H9)-derived HBC P0, HBC P10, or HBC clone into the hepatocyte-like cells is presented schematically. Details are described in Experimental Procedures.

(B) Phase-contrast micrographs of the HBC P10-derived hepatocyte-like cells are shown.

(C) The HBC P10-derived hepatocyte-like cells were subjected to immunostaining with anti-CYP3A4 (green), anti-αAT (red), and anti-ALB (red) antibodies.

(D and E) The gene expression levels of hepatocyte (D) or cholangiocyte (E) markers in HBC P0-, HBC P10-, or HBC clone-derived hepatocyte-like cells were measured by real-time RT-PCR after 14 days of hepatocyte differentiation. In (D), the gene expression levels in

(legend continued on next page)

cultured for 2 days on Matrigel (BD Biosciences) in differentiation hESF-DIF medium that contains 100 ng/ml Activin A (R&D Systems) (hESF-DIF medium was purchased from Cell Science & Technology Institute; differentiation hESF-DIF medium was supplemented with 10 μg/ml human recombinant insulin, 5 μg/ml human apotransferrin, 10 μM 2-mercaptoethanol, 10 μM ethanolamine, 10 μM sodium selenite, and 0.5 mg/ml bovine fatty acid free serum albumin [all from Sigma]). To generate definitive endoderm cells, the mesendoderm cells (day 2) were transduced with 3,000 vector particle (VP)/cell of FOXA2-expressing adenovirus vectors (Ad-FOXA2) for 1.5 hr and cultured until day 6 on Matrigel in differentiation hESF-DIF medium supplemented with 100 ng/ml Activin A. For induction of hepatoblasts, the definitive endoderm cells were cultured for 3 days on a Matrigel in differentiation hESF-DIF medium supplemented with 30 ng/ml bone morphogenetic protein 4 (BMP4) (R&D Systems) and 20 ng/ml FGF4 (R&D Systems).

Establishment and Maintenance of the hPSC-Derived HBCs

The hPSC-derived HBCs were first purified from the hPSC-derived cells (day 9) by selecting attached cells on a human recombinant LN111 (BioLamina)-coated dish at 15 min after plating. The hPSC-derived HBCs were cultured on a human LN111-coated dish (2.0×10^4 cells/cm^2) in maintenance DMEM/F12 medium (DMEM/F12 medium [Invitrogen] was supplemented with 10% FBS, 1 × insulin/transferrin/selenium, 10 mM nicotinamide, 10^{-7} M dexamethasone (DEX) (Sigma), 20 mM HEPES, 25 mM $NaHCO_3$, 2 mM L-glutamine, penicillin/streptomycin, 40 ng/ml hepatocyte growth factor [HGF] [R&D Systems] and 20 ng/ml epidermal growth factors [EGF] [R&D Systems]). The medium was refreshed every day. The hPSC-derived HBCs were dissociated with Accutase (Millipore) into single cells and subcultured every 6 or 7 days.

Establishment and Maintenance of a Single hPSC-Derived HBC

For single-cell culture, the single HBC was plated to separate well of human LN111-coated 96-well plate in maintenance DMEM/F12 medium supplemented with 25 μM Y-27632 (ROCK inhibitor) (Millipore), and then colonies derived from a single cell were manually picked up and cultured as well as HBCs (these cells were designated the HBC clone).

In Vitro Hepatocyte and Cholangiocyte Differentiation

To induce hepatocyte differentiation, the hPSC-derived HBC P0, HBC P10, and HBC clone were cultured for 14 days on a Matrigel-coated dish (7.5×10^4 cells/cm^2) in HCM (Lonza) supplemented with 20 ng/ml HGF, 20 ng/ml Oncostatin M (OsM) (R&D Systems), and 10^{-6} M DEX. To induce cholangiocyte differentiation, the hPSC-derived HBC P0, HBC P10, and HBC clone were cultured in collagen gel for 14 days. To establish collagen gel plates, 500 μl collagen gel solution (consisting of 400 μl type I-A Collagen (Nitta gelatin), 50 μl 10 × DMEM, and 50 μl of 200 mM HEPES buffer containing 2.2% $NaHCO_3$ and 0.05 M NaOH) was added to each well, and then the plates were incubated at 37°C for 30 min. The hPSC-derived HBC P0, HBC P10, and HBC clone (5×10^4 cells) were resuspended in 500 μl differentiation DMEM/F12 medium (differentiation DMEM/F12 medium was supplemented with 20 mM HEPES, 2 mM L-glutamine, 100 ng/ml EGF, and 40 ng/ml insulin-like growth factor 2 [ILGF2]), and then mixed with 500 μl of the collagen gel solution and plated onto the basal layer of collagen. After 30 min, 2 ml of differentiation DMEM/F12 medium was added to the well.

Ad Vectors

Ad vectors were constructed by an improved in vitro ligation method. The human EF-1α promoter-driven FOXA2-expressing Ad vectors (Ad-FOXA2) were constructed previously (Takayama et al., 2012b). All of Ad vectors contain a stretch of lysine residue (K7) peptides in the C-terminal region of the fiber knob for more efficient transduction of hESCs, hiPSCs, mesendoderm cells, and definitive endoderm cells, in which transfection efficiency was almost 100%, and purified as described previously (Inamura

PH 48 hr were taken as 1.0. In (E), the gene expression levels in HBC P10 (before differentiation) were taken as 1.0. Data represent the mean ± SD from three independent experiments. Student's t test indicated that gene expression levels of the hepatocyte markers in "after" were significantly higher than those in "before" ($p < 0.01$).

(F) The efficiency of hepatocyte differentiation was measured by estimating the percentage of ASGR1-positive cells using FACS analysis.

(G) The amounts of ALB (left) and urea (right) secretion were examined. Data represent the mean ± SD from three independent experiments. Student's t test indicated that the percentage of ASGR1-positive cells, the ALB secretion level, and urea secretion level in "after" were significantly higher than those in "before" ($p < 0.01$).

(H) The procedure for the differentiation of the hESC-derived HBC P0, HBC P10, or HBC clone into cholangiocyte-like cells is presented schematically. Details are described in Experimental Procedures.

(I) Phase-contrast micrographs of the HBC P10-derived cholangiocyte-like cells are shown.

(J) The HBC P10-derived cholangiocyte-like cells were subjected to immunostaining with anti-CK7 (red) antibodies.

(K and L) The gene expression levels of hepatocyte (K) or cholangiocyte (L) markers in the HBC P0-, HBC P10-, or HBC clone-derived cholangiocyte-like cells were measured by real-time RT-PCR after 14 days of cholangiocyte differentiation. In (K), the gene expression levels in PH 48 hr were taken as 1.0. In (L), the gene expression levels in HBC P10 (before cholangiocyte differentiation) were taken as 1.0. Data represent the mean ± SD from three independent experiments. Student's t test indicated that the gene expression levels of cholangiocyte markers in "after" were significantly higher than those in "before" ($p < 0.01$). "Before" indicates the HBCs before hepatocyte or cholangiocyte differentiation; "After" indicates the HBCs after hepatocyte or cholangiocyte differentiation.

See also Figures S4 and S5 and Tables S1–S4.

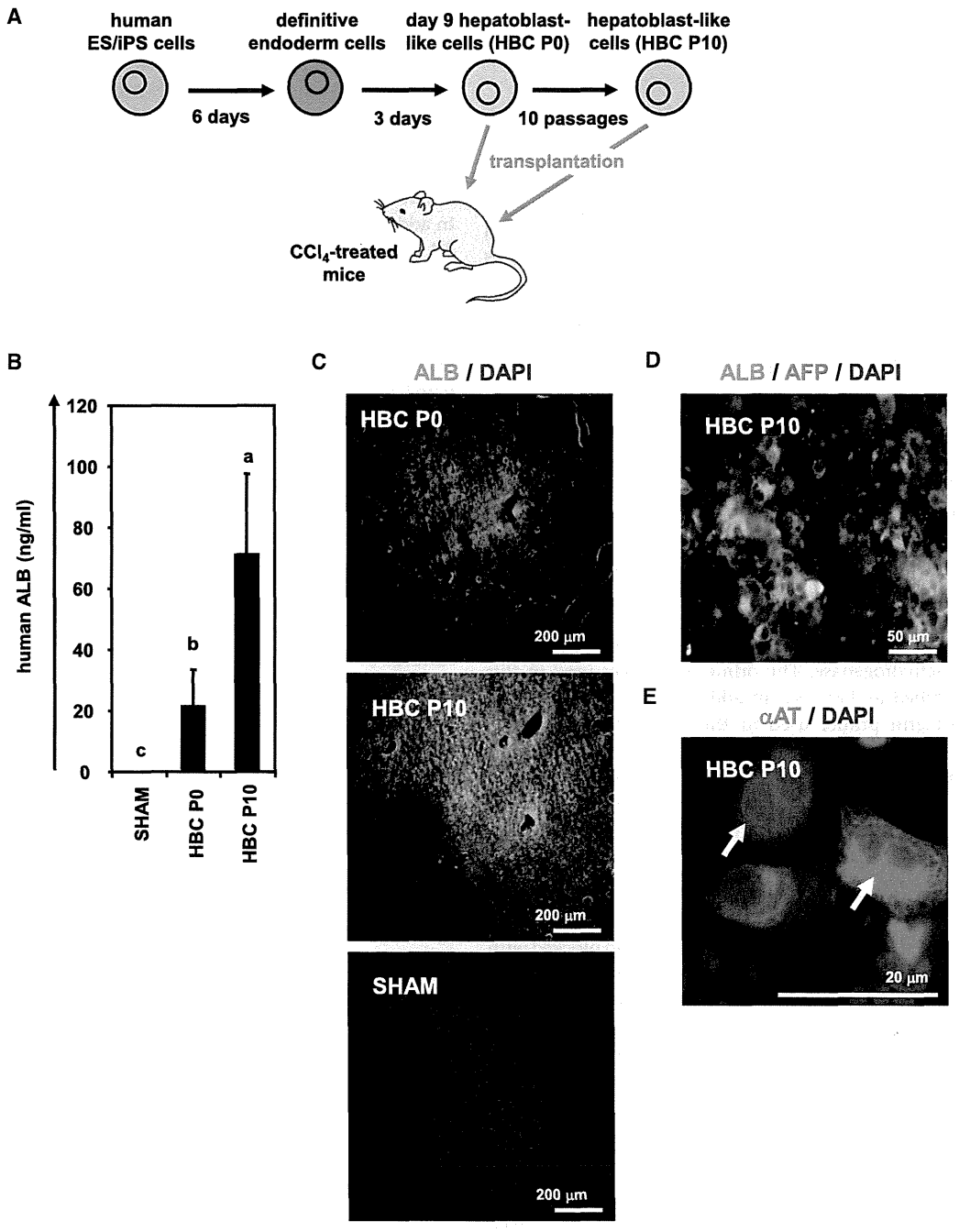

Figure 5. The hESC-Derived HBCs Were Integrated into the Mouse Liver Parenchyma

(A) The procedure for transplantation of the hESC (H9)-derived HBC P0 and HBC P10 into CCl_4 (4 ml/kg)-treated Rag2/IL2 receptor gamma double-knockout mice is presented schematically.

(B) The human ALB level in recipient mouse serum was measured at 2 weeks after transplantation. Data represent the mean ± SD from six to eight mice in each group. Statistical significance was evaluated by ANOVA followed by Bonferroni post hoc tests to compare all groups. Groups that do not share the same letter are significantly different from each other ($p < 0.05$).

(C) Expressions of the ALB (green) in the liver of transplanted mice were examined by immunohistochemistry at 2 weeks after transplantation.

(D and E) The expressions of AFP (red), ALB (green) (D), and αAT (red) (E) were examined by immunohistochemistry at 2 weeks after hESC-derived HBC P10 transplantation. White arrows show transplanted cells, which have double nuclei.

See also Tables S2 and S3.

et al., 2011; Takayama et al., 2011; Tashiro et al., 2010). The VP titer was determined by using a spectrophotometric method.

Flow Cytometry

Single-cell suspensions of the hPSC-derived cells were fixed with 4% paraformaldehyde (PFA) at 4°C for 10 min and then incubated with the primary antibody (described in Table S2), followed by the secondary antibody (described in Table S3). Control cells were incubated with anti-mouse, goat, or rabbit immunoglobulin (Ig) G antibodies (Santa Cruz Biotechnology) and then incubated with the secondary antibody. Flow cytometry analysis was performed using a fluorescence-activated cell sorting (FACS) LSR Fortessa flow cytometer (BD Biosciences). Cell sorting was performed using a FACS Aria (BD Biosciences).

RNA Isolation and RT-PCR

Total RNA was isolated from hPSCs and their derivatives using ISOGENE (Nippon Gene). cDNA was synthesized using 500 ng of total RNA with a Superscript VILO cDNA synthesis kit (Invitrogen). Real-time RT-PCR was performed with SYBR green PCR Master Mix (Applied Biosystems) using an Applied Biosystems StemOnePlus real-time PCR systems. Relative quantification was performed against a standard curve, and the values were normalized against the input determined for the housekeeping gene, glyceraldehyde 3-phosphate dehydrogenase. The primer sequences used in this study are described in Table S4. In addition, we confirmed that every beta integrin primer used in this manuscript showed a similar amplification efficacy (Table S5). The amplification efficiency was calculated from the slope of the standard curve according to the following formula: e = 10^(−1/slope)-1. Every beta integrin primer used in this manuscript showed a similar amplification efficacy.

Immunohistochemistry

The cells were fixed with 4% PFA for 15 min and then blocked with PBS containing 2% FBS, 2% bovine serum albumin (BSA), and 0.1% Triton X-100 (Wako Pure Chemicals Industries) for 1 hr. The cells were incubated with primary antibody (described in Table S2) at 4°C for overnight, followed by incubation with a secondary antibody (described in Table S3) at room temperature for 1 hr. Nuclei were counterstained with DAPI (blue).

ELISA

The hPSC-derived HBC P0, HBC P10, and HBC clone were differentiated into the hepatocyte-like cells as described in Figure 4A. The culture supernatants, which were incubated for 24 hr after fresh medium was added, were collected and analyzed for the amount of ALB secretion by ELISA. ELISA kits for ALB were purchased from Bethyl Laboratories. The amount of ALB secretion was calculated according to each standard followed by normalization to the protein content per well. The human ALB amount in mice serum was also examined by ELISA.

Transplantation of the hESC-Derived HBCs

The hESC-derived HBCs were dissociated using accutase and then suspended with maintenance DMEM/F12 medium without serum. Eight- to 10-week-old Rag2/IL2Rg double-knockout mice were prepared. The hESC-derived HBCs (1×10^6 cells) were transplanted 24 hr after administration of CCl_4 (4 ml/kg) by intrasplenical injection. Recipient mouse liver and blood were harvested at 2 weeks after transplantation. The livers were fixed with 4% PFA and processed for immunohistochemistry. Human hepatocytes producing the ALB, AFP, and αAT protein were identified in mouse liver by an antibody specifically recognizing human but not mouse albumin. In addition, serum was extracted and subjected to ELISA analysis. All animal experiments were conducted in accordance with institutional guidelines.

Urea Secretion

The hPSC-derived HBC P0, HBC P10, and HBC clone were differentiated into hepatocyte-like cells as described in Figure 4A. The culture supernatants, which were incubated for 24 hr after fresh medium was added, were collected and analyzed for the amount of urea secretion. The urea measurement kits were purchased from BioAssay Systems. The amount of urea secretion was calculated according to each standard followed by normalization to the protein content per well. In Figure S5B, both the HBC-derived hepatocyte-like cells and primary human hepatocytes (PHs) (three lots of cryopreserved human hepatocytes were used), that were cultured for 48 hr after the cells were plated (PH 48 hr), were cultured in HCM (containing glutamine) or DMEM (not containing glutamine; Wako) in the presence or absence of 1 mM ammonium chloride (NH_4Cl, Wako) for 24 hr, and then the amount of urea secretion was measured.

Primary Human Hepatocytes

Three lots of cryopreserved human hepatocytes (lot Hu8072 [CellzDirect], HC2-14, and HC10-101 [Xenotech]) were used. The vials of hepatocytes were rapidly thawed in a shaking water bath at 37°C; the contents of the vial were emptied into prewarmed Cryopreserved Hepatocyte Recovery Medium (Gibco) and the suspension was centrifuged at 100 g for 10 min at room temperature. The hepatocytes were seeded at 1.25×10^5 cells/cm^2 in HCM (Lonza) containing 10% fetal calf serum (FCS) (Gibco) onto type I collagen-coated 12-well plates. The medium was replaced with hepatocyte culture medium containing 10% FCS 6 hr after seeding. The hepatocytes, which were cultured 48 hr after plating the cells, were used in the experiments.

Adhesion-Blocking Assay Using Integrin Antibody

Twelve-well plates were coated with human recombinant LN111, 211, 411, or 511 (all from BioLamina) and blocked by 1% heat-denatured BSA containing PBS. The hESC-derived single cells were incubated with function-blocking antibodies to integrin α6 and β1 (at the concentrations as recommended by the manufacturer) for 30 min, plated on a human LN111-coated 12-well dish, and allowed to adhere for 1 hr at 37°C. After unattached cells were removed, the remaining adherent cells were fixed for 20 min with 5% glutaraldehyde. The hESC-derived cells that had adhered to the wells were stained with 200 μl of 0.3% crystal violet (Wako) solution at room temperature for 15 min. Excess crystal violet was then removed, and the wells were washed three times. Fixed crystal violet was solubilized in 200 μl of 100% ethanol at room

temperature for 15 min. Cell viability was estimated by measuring the absorbance at 595 nm of each well using a microtiter plate reader (Sunrise, Tecan).

CYP Activity

To measure the CYP1A2, 2C9, and 3A4 activity of the cells, we performed lytic assays by using P450-GloTM CYP1A2, 2C9, and 3A4 Assay Kits (Promega), respectively. We measured the fluorescence activity with a luminometer (Lumat LB 9507; Berthold) according to the manufacturer's instructions. The CYP activity was normalized with the protein content per well.

Karyotyping

This experiment was carried out at Chromosome Science Labo.

Cell Viability Tests

Cell viability was assessed by using a WST-8 assay kit (Dojindo), and the results are presented in Figure S5C. After treatment with test compounds, such as acetaminophen (Wako) and troglitazone (Wako) for 24 hr, the cell viability was measured. The control cells were incubated in the absence of test compounds and were considered to have 100% viability value. Controls were treated with DMSO (final concentration 0.1%).

SUPPLEMENTAL INFORMATION

Supplemental Information includes five figures and five tables and can be found with this article online at http://dx.doi.org/10.1016/j.stemcr.2013.08.006.

ACKNOWLEDGMENTS

We thank Yasuko Hagihara for her excellent technical support. H.M., K.K., and T.H. were supported by grants from the Ministry of Health, Labor, and Welfare of Japan. H.M. was also supported by the Project for Technological Development of the Japan Science and Technology Agency (JST) and by the Uehara Memorial Foundation. F.S. was supported by Program for Promotion of Fundamental Studies in Health Sciences of the National Institute of Biomedical Innovation. K.T. and Y.N. are Research Fellows of the Japan Society for the Promotion of Science.

Received: June 6, 2013
Revised: August 27, 2013
Accepted: August 27, 2013
Published: October 3, 2013

REFERENCES

Clément, B., Rescan, P.Y., Baffet, G., Loréal, O., Lehry, D., Campion, J.P., and Guillouzo, A. (1988). Hepatocytes may produce laminin in fibrotic liver and in primary culture. Hepatology *8*, 794–803.

Couvelard, A., Bringuier, A.F., Dauge, M.C., Nejjari, M., Darai, E., Benifla, J.L., Feldmann, G., Henin, D., and Scoazec, J.Y. (1998). Expression of integrins during liver organogenesis in humans. Hepatology *27*, 839–847.

Hay, D.C., Zhao, D., Fletcher, J., Hewitt, Z.A., McLean, D., Urruticoechea-Uriguen, A., Black, J.R., Elcombe, C., Ross, J.A., Wolf, R., and Cui, W. (2008). Efficient differentiation of hepatocytes from human embryonic stem cells exhibiting markers recapitulating liver development in vivo. Stem Cells *26*, 894–902.

Inamura, M., Kawabata, K., Takayama, K., Tashiro, K., Sakurai, F., Katayama, K., Toyoda, M., Akutsu, H., Miyagawa, Y., Okita, H., et al. (2011). Efficient generation of hepatoblasts from human ES cells and iPS cells by transient overexpression of homeobox gene HEX. Mol. Ther. *19*, 400–407.

Kamiya, A., Kakinuma, S., Yamazaki, Y., and Nakauchi, H. (2009). Enrichment and clonal culture of progenitor cells during mouse postnatal liver development in mice. Gastroenterology *137*, 1114–1126.

Liu, H., Kim, Y., Sharkis, S., Marchionni, L., and Jang, Y.Y. (2011). In vivo liver regeneration potential of human induced pluripotent stem cells from diverse origins. Sci. Transl. Med. *3*, 82ra39.

Makino, H., Toyoda, M., Matsumoto, K., Saito, H., Nishino, K., Fukawatase, Y., Machida, M., Akutsu, H., Uyama, T., Miyagawa, Y., et al. (2009). Mesenchymal to embryonic incomplete transition of human cells by chimeric OCT4/3 (POU5F1) with physiological co-activator EWS. Exp. Cell Res. *315*, 2727–2740.

Nagata, S., Toyoda, M., Yamaguchi, S., Hirano, K., Makino, H., Nishino, K., Miyagawa, Y., Okita, H., Kiyokawa, N., Nakagawa, M., et al. (2009). Efficient reprogramming of human and mouse primary extra-embryonic cells to pluripotent stem cells. Genes Cells *14*, 1395–1404.

Paku, S., Schnur, J., Nagy, P., and Thorgeirsson, S.S. (2001). Origin and structural evolution of the early proliferating oval cells in rat liver. Am. J. Pathol. *158*, 1313–1323.

Rodin, S., Domogatskaya, A., Ström, S., Hansson, E.M., Chien, K.R., Inzunza, J., Hovatta, O., and Tryggvason, K. (2010). Long-term self-renewal of human pluripotent stem cells on human recombinant laminin-511. Nat. Biotechnol. *28*, 611–615.

Schmelzer, E., Zhang, L., Bruce, A., Wauthier, E., Ludlow, J., Yao, H.L., Moss, N., Melhem, A., McClelland, R., Turner, W., et al. (2007). Human hepatic stem cells from fetal and postnatal donors. J. Exp. Med. *204*, 1973–1987.

Sumi, T., Tsuneyoshi, N., Nakatsuji, N., and Suemori, H. (2008). Defining early lineage specification of human embryonic stem cells by the orchestrated balance of canonical Wnt/beta-catenin, Activin/Nodal and BMP signaling. Development *135*, 2969–2979.

Takayama, K., Inamura, M., Kawabata, K., Tashiro, K., Katayama, K., Sakurai, F., Hayakawa, T., Furue, M.K., and Mizuguchi, H. (2011). Efficient and directive generation of two distinct endoderm lineages from human ESCs and iPSCs by differentiation stage-specific SOX17 transduction. PLoS ONE *6*, e21780.

Takayama, K., Inamura, M., Kawabata, K., Katayama, K., Higuchi, M., Tashiro, K., Nonaka, A., Sakurai, F., Hayakawa, T., Furue, M.K., and Mizuguchi, H. (2012a). Efficient generation of functional hepatocytes from human embryonic stem cells and induced pluripotent stem cells by HNF4α transduction. Mol. Ther. *20*, 127–137.

Takayama, K., Inamura, M., Kawabata, K., Sugawara, M., Kikuchi, K., Higuchi, M., Nagamoto, Y., Watanabe, H., Tashiro, K., Sakurai,

F., et al. (2012b). Generation of metabolically functioning hepatocytes from human pluripotent stem cells by FOXA2 and HNF1α transduction. J. Hepatol. *57*, 628–636.

Takayama, K., Kawabata, K., Nagamoto, Y., Kishimoto, K., Tashiro, K., Sakurai, F., Tachibana, M., Kanda, K., Hayakawa, T., Furue, M.K., and Mizuguchi, H. (2013). 3D spheroid culture of hESC/hiPSC-derived hepatocyte-like cells for drug toxicity testing. Biomaterials *34*, 1781–1789.

Tanimizu, N., Saito, H., Mostov, K., and Miyajima, A. (2004). Long-term culture of hepatic progenitors derived from mouse Dlk+ hepatoblasts. J. Cell Sci. *117*, 6425–6434.

Tashiro, K., Kawabata, K., Inamura, M., Takayama, K., Furukawa, N., Sakurai, F., Katayama, K., Hayakawa, T., Furue, M.K., and Mizuguchi, H. (2010). Adenovirus vector-mediated efficient transduction into human embryonic and induced pluripotent stem cells. Cell Reprogram. *12*, 501–507.

Tateno, C., Yoshizane, Y., Saito, N., Kataoka, M., Utoh, R., Yamasaki, C., Tachibana, A., Soeno, Y., Asahina, K., Hino, H., et al. (2004). Near completely humanized liver in mice shows human-type metabolic responses to drugs. Am. J. Pathol. *165*, 901–912.

Zhang, L., Theise, N., Chua, M., and Reid, L.M. (2008). The stem cell niche of human livers: symmetry between development and regeneration. Hepatology *48*, 1598–1607.

Zhao, D., Chen, S., Cai, J., Guo, Y., Song, Z., Che, J., Liu, C., Wu, C., Ding, M., and Deng, H. (2009). Derivation and characterization of hepatic progenitor cells from human embryonic stem cells. PLoS ONE *4*, e6468.

PLOS | ONE

Myosin II ATPase Activity Mediates the Long-Term Potentiation-Induced Exodus of Stable F-Actin Bound by Drebrin A from Dendritic Spines

Toshiyuki Mizui[1,3], Yuko Sekino[1,2*¤a], Hiroyuki Yamazaki[1], Yuta Ishizuka[1], Hideto Takahashi[1¤b], Nobuhiko Kojima[1], Masami Kojima[2,3], Tomoaki Shirao[1*]

1 Department of Neurobiology and Behavior, Gunma University Graduate School of Medicine, Maebashi, Gunma, Japan, **2** Core Research for Evolution Science and Technology, Japan Science and Technology Corporation, Kawaguchi, Saitama, Japan, **3** Bio-interface Research Group, Health Research Institute, National Institute of Advanced Industrial Science and Technology (AIST), Ikeda, Osaka, Japan

Abstract

The neuronal actin-binding protein drebrin A forms a stable structure with F-actin in dendritic spines. NMDA receptor activation causes an exodus of F-actin bound by drebrin A (DA-actin) from dendritic spines, suggesting a pivotal role for DA-actin exodus in synaptic plasticity. We quantitatively assessed the extent of DA-actin localization to spines using the spine-dendrite ratio of drebrin A in cultured hippocampal neurons, and found that (1) chemical long-term potentiation (LTP) stimulation induces rapid DA-actin exodus and subsequent DA-actin re-entry in dendritic spines, (2) Ca^{2+} influx through NMDA receptors regulates the exodus and the basal accumulation of DA-actin, and (3) the DA-actin exodus is blocked by myosin II ATPase inhibitor, but is not blocked by myosin light chain kinase (MLCK) or Rho-associated kinase (ROCK) inhibitors. These results indicate that myosin II mediates the interaction between NMDA receptor activation and DA-actin exodus in LTP induction. Furthermore, myosin II seems to be activated by a rapid actin-linked mechanism rather than slow MLC phosphorylation. Thus the myosin-II mediated DA-actin exodus might be an initial event in LTP induction, triggering actin polymerization and spine enlargement.

Citation: Mizui T, Sekino Y, Yamazaki H, Ishizuka Y, Takahashi H, et al. (2014) Myosin II ATPase Activity Mediates the Long-Term Potentiation-Induced Exodus of Stable F-Actin Bound by Drebrin A from Dendritic Spines. PLoS ONE 9(1): e85367. doi:10.1371/journal.pone.0085367

Editor: Makoto Sato, Osaka University Graduate School of Medicine, Japan

Received September 30, 2013; **Accepted** November 25, 2013; **Published** January 22, 2014

Funding: This work was supported by Grants-in-Aid for Scientific Research (16300117, 19200029) and on Priority Areas - Elucidation of neural network function in the brain - from the Ministry of Education, Culture, Sports, Science and Technology of Japan (20021002). The funders had no role in study design, data collection and analysis, decision to publish, or preparation of the manuscript.

Competing Interests: The authors have declared that no competing interests exist.

* E-mail: yukos@nihs.go.jp (YS); tshirao@ gunma-u.ac.jp (TS)

¤a Current address: Division of Pharmacology, National Institute of Health Sciences, Setagaya-ku, Tokyo, Japan
¤b Current address: Institut de recherches cliniques de Montréal (IRCM), Université de Montréal (UdeM), Québec, Canada

Introduction

Drebrin A is a neuron-specific actin-binding protein that is located at the base of dendritic spine heads [1–3]. Drebrin A binding modifies the pitch of actin filaments [4–5] and forms stable F-actin that is resistant to depolymerization by cytochalasin D [6–7]. Mikati *et al* [8] have recently shown that F-actin that is bound by drebrin A (DA-actin) is stable, and the depolymerization of DA-actin is suppressed at both ends of the filaments. In developing neurons, DA-actin is not observed in dynamic dendritic filopodia, but is observed in more stable dendritic spines [9]. Furthermore, DA-actin is suitable for the formation of a stable higher-order F-actin structure (DA-actin complex), because drebrin A has two F-actin-binding domains that can act cooperatively to enable interfilament interactions [10]. Together, it is suggested that DA-actin forms stable structures of F-actin at the base of dendritic spine heads.

Dendritic spines at rest contain a dynamic F-actin pool that shows quick treadmilling, and a stable pool that shows slow treadmilling. The dynamic pool is observed at the tip of the spine head, whereas the stable pool is located at the base of the spine head [11]. The aforementioned stability and localization of DA-actin suggest that DA-actin is a major component of the stable F-actin pool in dendritic spines, whereas F-actin that is not bound by drebrin A (non-DA-actin) is a major component of the dynamic F-actin pool (for review, see Shirao and González-Billault [12]).

We have previously shown that NMDA receptor activation induces the loss of drebrin A from dendritic spines [13]. Because our previous biochemical analyses revealed that most drebrin A in neurons is bound to F-actin (for a review, see Sekino *et al* [14]), we can extrapolate DA-actin localization from drebrin immunostaining images. Furthermore, fluorescence recovery after photobleaching analysis has demonstrated that drebrin A dynamics in spines are far slower than those of monomeric proteins such as monomeric actin [15] and cortactin [16], indicating that drebrin A remains bound to F-actin even when drebrin A dynamically changes its localization [17]. Together, it is suggested that NMDA receptor activation induces the DA-actin exodus from dendritic spines. However, the mechanism by which NMDA receptor activation links to the DA-actin exodus remains to be elucidated.

It has recently been reported that myosin II ATPase activity is necessary for actin reorganization during long-term potentiation (LTP) induction [18]. We have previously shown that myosin II is

contained in the DA-actin complex [19], but the interaction between myosin II and DA-actin is suppressed in the DA-actin complex [20]. The release of the actomyosin interaction leads to the activation of myosin II ATPase, resulting in reorganization of the actin cytoskeleton through severing of F-actin [21]. Therefore, LTP stimulation might disinhibit the suppressed actomyosin interaction, resulting in the activation of myosin II ATPase.

In this study, we quantitatively assessed the extent to which DA-actin localizes to dendritic spines, clarified DA-actin migration in the context of synaptic plasticity and examined whether myosin II mediates the interaction between NMDA receptor activation and DA-actin exodus.

Materials and Methods

All animal experiments were performed with the permission of the Animal Care and Experimentation Committee, Gunma University, Showa Campus (Maebashi, Japan). All efforts were made to minimize animal suffering and reduce the number of animals used in this study.

Reagents

4-aminopyridine (4-AP) and pyruvate were purchased from Sigma (St. Louis, MO, USA). Hexahydro-1-[(5-iodo-1-naphthalenyl) sulfonyl]-1*H*-1,4-diazepine hydrochloride (ML-7) and (*S*)-(+)-2-Methyl-1-[(4-methyl-5-isoquinolinyl)sulfonyl]-hexahydro-1*H*-1,4-diazepine dihydrochloride (H-1152) were purchased from Calbiochem (San Diego, CA, USA). Ethyleneglycol-*bis* (β-aminoethyl)-N,N,N',N'-tetraacetic acid (EGTA) was purchased from Dojin (Kumamoto, Japan). Tetrodotoxin (TTX) was purchased from Wako (Osaka, Japan). D-(−)-2-amino-5-phosphonopentanoic acid (APV), bicuculline, (S)-(−)-blebbistatin, (R)-(+)-blebbistatin, thapsigargin and nifedipine were purchased from Tocris (Ellisville, MO, USA).

Hippocampal neuron cultures

Timed pregnant Wistar rats (Charles River Laboratories Inc., Yokohama, Japan) were deeply anesthetized with diethyl ether and sacrificed by decapitation. Hippocampi were dissected from the fetuses at embryonic day 18. The hippocampal cells were prepared by trypsinization and mechanical dissociation according to previously described methods [9]. Briefly, the cell suspensions were plated at a density of 5000 cells/cm^2 on coverslips coated with poly-L-lysine (Sigma). Cells were incubated in Minimum Essential Medium (MEM; Invitrogen, San Diego, CA, USA) supplemented with 10% fetal bovine serum (Invitrogen), 0.6% glucose (Wako), and 1 mM pyruvate (Sigma). After the cells achieved attachment, the coverslips were transferred to a culture dish containing a glial monolayer and maintained in normal medium consisting of serum-free MEM, 2% B27 supplement (Invitrogen), 0.6% glucose, and 1 mM sodium pyruvate at 35.8°C in a humidified incubator with 5% CO_2 for 21 days *in vitro* (DIV). Cytosine β-D-arabinofuranoside (10 μM; Sigma) was added to the cultures at 4 DIV to inhibit glial proliferation.

Pharmacological treatments

The chemical LTP (cLTP) stimulation solution used in this study was Mg^{2+}-free Tyrode's solution supplemented with 200 μM glycine, 20 μM bicuculline, 1 μM strychnine and 0.5 μM TTX [22]. For cLTP induction, the neurons were preincubated in cLTP stimulation solution without 200 μM glycine for 20 min, and then stimulated with glycine for the indicated amount of time.

For blocker experiments, the neurons were preincubated in medium supplemented with blocker for 30 min and then stimulated with cLTP stimulation solution or 100 μM glutamate in the presence of each blocker for the indicated amount of time. For the stimulation studies with 90 mM potassium chloride, the neurons were preincubated in Tyrode's solution (119 mM NaCl, 2.5 mM KCl, 2 mM $CaCl_2$, 2 mM $MgSO_4$, 25 mM HEPES [pH 7.4], and 30 mM glucose).

Immunocytochemistry

After three weeks *in vitro*, cells were fixed in 4% paraformaldehyde with 0.1% glutaraldehyde in phosphate-buffered saline (PBS; pH 7.4) at 4°C for 10 min. The fixed cells were permeabilized with 0.1% Triton X-100 in PBS for 3 min and then incubated in blocking solution (3% bovine serum albumin in PBS) for 1 h, followed by an overnight incubation with primary antibodies at 4°C. A monoclonal antibody against drebrin (clone M2F6, hybridoma supernatant [23]) was used at a 1:1 dilution. F-actin was detected with rhodamine-conjugated phalloidin (Molecular Probes, Eugene, OR, USA). After being washed with PBS for 30 min, the cells were incubated for 1 h at room temperature with secondary antibodies. Anti-mouse IgG antibodies conjugated to fluorescein (Cappel, West Chester, PA, USA) were used to detect the monoclonal antibodies against drebrin. After being washed with PBS, the cells were mounted on glass slides with Perma Fluor mounting medium (Thermo Shandon, Pittsburgh, PA, USA).

Labeling of surface GluR1 was performed according to previous reports [22,24] with minor modifications. Briefly, after the cLTP stimulation, surface GluR1 was labeled in live neurons by 30 min incubation with a rabbit polyclonal antibody against the N-terminus of the GluR1 subunit (PC246, 1:15 dilution in glial conditioned media; Calbiochem). After washout of the antibody with Hank's balanced salt solution, the neurons were fixed in 2% PFA for 20 min at 4°C without permeabilization. The surface receptors were visualized using a fluorescein-conjugated goat anti-rabbit secondary antibody (Cappel).

Fluorescence microscopy

All fluorescence images were obtained on a Zeiss Axioplan 2 microscope (Zeiss, Jena, Germany) equipped with a Cool Snap fx CCD camera (Photometrics, Tucson, AZ, USA), a 63×, 1.4 numerical aperture objective lens (Zeiss), and MetaMorph software (Universal Imaging, West Chester, PA, USA). A filter set (86000 Sedat Quad; Chroma, Brattleboro, VT, USA) was mounted in the excitation and emission filter wheels (Ludl Electronic Products, Hawthorne, NY, USA) of the microscope. All data were collected at 1300×1030 resolution at 12 bits/pixel. A single pixel in the image corresponded to a 106 nm^2 area in the specimen plane. The images used for comparison in this study were collected under identical conditions. The captured fluorescence images were analyzed using the MetaMorph program. The GFP, rhodamine, and Cy5 signals were obtained through filters for FITC, Cy3, and Cy5, respectively. We found no fluorescence leakage of these signals through the other filters. The images presented in this study were prepared using Adobe Photoshop software (Adobe Systems, San Jose, CA, USA).

Plasmids and Transfection

Construction of the green fluorescent protein-tagged drebrin A (GFP-DA) has been described previously [25]. At 7 DIV, the hippocampal neurons were transfected with plasmids using a calcium phosphate coprecipitation protocol [26]. Two weeks after transfection, the transfected neurons were analyzed using time-lapse imaging.

Time-lapse imaging

Live time-lapse imaging was performed at 35.8°C on a Zeiss inverted microscope stage using a temperature-controlled chamber with continuous perfusion, as described previously [7]. Briefly, the cell cultures were mounted in a chamber containing Mg^{2+}-free Tyrode's solution supplemented with 20 μM bicuculline, 1 μM strychnine and 0.5 μM TTX. The chamber was maintained and perfused with the same solution. The perfusing solution (1 ml/min) was switched between the control and cLTP stimulation medium using a hydraulic two-way valve switch with a dead space of 3.5 ml between the switch and the bath. Thus, the test medium would reach the chamber 210 sec after flipping the switch (data not shown). The time-lapse images were acquired at 10 sec intervals for 20 min using MetaMorph software.

Image analysis and quantification

All quantifications were performed by an observer who was blind to the experimental conditions, and the morphological analysis was performed using the MetaMorph software. Each experiment was repeated at least three times with independent neuronal preparations.

For quantification, spiny neurons with pyramidal morphology were selected from at least three separate cultures. In our hippocampal cultures, we have previously shown that pyramidal neurons are multipolar cells with a large soma and multiple thick dendritic processes [27]. Therefore, we considered that these multipolar cells were hippocampal pyramidal neurons. Although the hippocampal culture also contains a variety of interneurons, they are comparatively few in number and most are morphologically distinguishable in culture [28].

To measure the surface cluster density of GluR1, the number of GluR1 clusters was measured according to previously described methods [24,29] with minor modifications. Briefly, the surface GluR1 signals were thresholded with intensity at two-fold the dendritic background to mark surface clusters of GluR1 using MetaMorph software. The surface clusters were selected using the 'regions' tool and analyzed using the 'integrated morphometry' feature. Next, the length of the analyzed region on a dendrite was measured. The density of surface GluR1 clusters were obtained by dividing the number of surface GluR1 clusters within a selected dendritic region by the length of the dendrite (50–100 μm total dendritic length per neuron).

Calculation of the spine-dendrite ratio

The spine-dendrite ratio (SDR) used in this study was the average fluorescence signal of the molecule of interest in a dendritic spine head divided by the average fluorescence signal of that molecule in the dendritic shaft at the foot of the spine. To measure the SDR, a single dendrite located between the cell soma and the second branch point (30–80 μm total dendritic length per neuron) was selected from each neuron. The dendritic spines and the shaft in the selected region were outlined on the F-actin fluorescence images, and circles (0.26 μm^2) were drawn at dendritic spine heads and at the foot of the spine in a dendritic shaft, using the 'ellipse region' tool of the MetaMorph software (Fig. 1A). Next, the average fluorescence intensity in each circle (calculated from the fluorescence signal intensity values) was measured using the 'region measurements' tool in the MetaMorph software. The number of spines measured were between 25 and 80 per neuron. The average SDR of spines per neuron was then calculated. The drebrin immunostaining and rhodamine-phalloidin signal intensity values were used to calculate the drebrin and F-actin SDRs, respectively.

Statistical analysis

The statistical analysis included a one-way ANOVA followed by a post hoc Scheffe's test. A Student's t test was performed for comparisons between control and drug-treated neurons. All data were presented as mean ± s.e.m. A p value of <0.01 was considered significant. The statistical analysis was performed using Microsoft Excel (Redmond, WA, USA).

Results

Quantitative assessment of DA-actin in dendritic spines

We used the spine-dendrite ratio (SDR) of drebrin immunostaining intensity to monitor the amounts of DA-actin in dendritic spines. We used the SDR of rhodamine-phalloidin staining intensity to assess the amount of total F-actin. The SDR used in this study is the average fluorescence signal of the molecule of interest in a dendritic spine head divided by the average fluorescence signal of that molecule in the dendritic shaft at the foot of the spine (Fig. 1A). The drebrin SDR of control cultured hippocampal neurons at 21 days *in vitro* (DIV) was 1.65±0.03 (n = 170 cells), whereas the actin SDR was 1.67±0.02 (n = 170 cells; Fig. 1B), demonstrating that both DA-actin and total F-actin accumulate more in the dendritic spines than the parent dendrites.

Chemical LTP stimulation induces a transient DA-actin exodus

Stimulation with chemical LTP (cLTP) solution for 3 min induced a significant increase in the glutamate receptor subunit 1 (GluR1) cluster density 30 min after treatment (Fig. 2). This increase was inhibited with 50 μM 2-amino-5-phosphonopentanoate (APV), an NMDA receptor blocker (Fig. 2). These data are consistent with an earlier study showing facilitated insertion of α-amino-3-hydroxy-5-methyl-4-isoxazolepropionic acid (AMPA) receptors during cLTP [22].

We examined whether cLTP stimulation would induce DA-actin to exit dendritic spines. At 5 min after cLTP stimulation, the intensity of drebrin immunostaining in dendritic spines was weak, but after 30 min the intensity was similar to that in untreated cells (Fig. 3A). Quantitative analysis showed that both drebrin and actin SDRs were significantly lower at 5 min but recovered after 30 min (Fig. 3B).

To analyze the time course of the DA-actin migration, we transfected a GFP-drebrin A-expressing vector into cultured hippocampal neurons and performed time-lapse imaging. The GFP-drebrin A SDR was transiently decreased following cLTP stimulation, similar to that of the native drebrin A (Fig. 3C). The GFP-drebrin A SDR began to decrease immediately after the neurons were exposed to cLTP solution (arrow in Fig. 3D) and then further declined throughout the period of stimulation. When the stimulation medium was switched back to control medium, the SDR began to rise and returned to the control level in 11 min after the completion of cLTP stimulation (Fig. 3D).

cLTP-induced DA-actin exodus is dependent on myosin II activity

Neurons were pretreated with 100 μM (S)-(−)-blebbistatin (aBL, the active form of blebbistatin), a myosin II ATPase blocker, for 30 min [30]. In the presence of aBL, cLTP stimulation did not affect the localization of either drebrin or actin in dendritic spines (photomicrographs in Fig. 4), and failed to decrease the drebrin and actin SDRs (n = 30 cells; p = 0.37 for drebrin SDR at 5 min, p = 0.34 for actin SDR; Student's *t* test; graphs in Fig. 4). This result indicates that myosin II activity is involved in the DA-actin

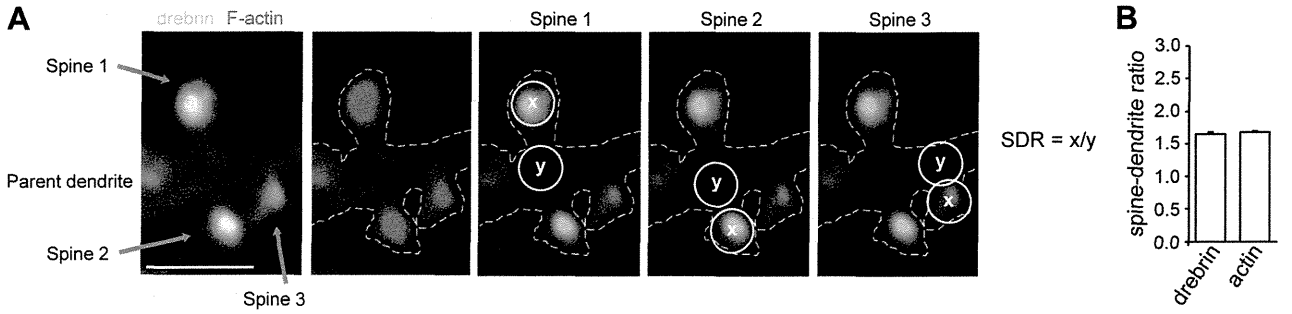

Figure 1. Spine-dendrite ratios of drebrin and actin. (**A**) Fluorescence images of drebrin (green) and F-actin (red) in control hippocampal neurons. The dendritic spines and the parent dendrite in the selected region were outlined on the F-actin fluorescence images (white dotted lines). Scale bar, 2 μm. Circles (0.26 μm^2, yellow) were drawn at the spine head and at the parent dendrite, and the average fluorescence intensities within the circles were measured. The SDR of each spine was obtained by dividing the average intensity of the dendritic spine by that of the parent dendrite. (**B**) The SDR per neuron was obtained as the average SDR of the spines. Bar graph shows the drebrin and actin SDRs of 21-DIV hippocampal neurons (n = 170 cells). Error bars represent s.e.m.
doi:10.1371/journal.pone.0085367.g001

exodus. The inactive form of blebbistatin (iBL) was used as a control. In the presence of iBL, cLTP stimulation significantly decreased the drebrin and actin SDRs.

Various kinds of stimulation induce DA-actin exodus

We stimulated cultured hippocampal neurons with 100 μM glutamate for 10 min, and fixed them immediately after the stimulation. This treatment induced the loss of drebrin and F-actin from dendritic spines (photomicrographs in Fig. 5A). On the other hand, it did not affect the density of spines or presynaptic terminals (Fig. S1). Quantitative analyses showed significant reductions in both the drebrin and actin SDRs (graphs in Fig. 5A).

We then examined whether other kinds of excitatory stimulation affect DA-actin localization. Increased spontaneous firing rates resulting from a 30-minute application of 50 μM bicuculline, a $GABA_A$ receptor blocker, combined with 500 μM 4-aminopyridine, a potassium channel blocker [31], induced a loss of drebrin and F-actin from dendritic spines (photomicrographs in Fig. 5B). A similar decrease was induced by membrane depolarization resulting from a 5-minute application of 90 mM KCl (photomicrographs in Fig. 5C). Quantitative analyses showed that both treatments significantly decreased the drebrin and actin SDRs (graphs in Fig. 5B, C). These data indicate that in addition to cLTP stimulation, various kinds of excitatory stimulation induce a DA-actin exodus.

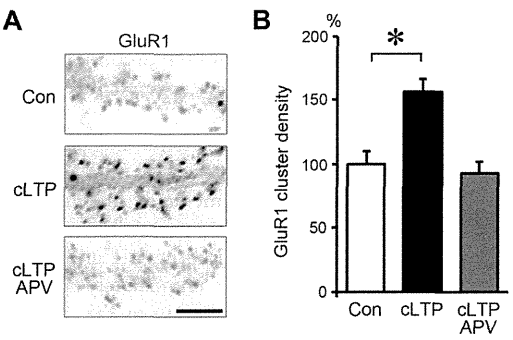

Figure 2. Increase in surface GluR1 immunostaining after chemical LTP (cLTP) stimulation. Neurons (21 DIV) were stimulated with buffer containing 0 μM Mg^{2+}, 200 μM glycine, 20 μM bicuculline, 1 μM strychnine and 0.5 μM TTX (cLTP stimulation) for 3 min. (**A**) Surface GluR1 was labeled before the stimulation (top panel; Con) or 30 min after the stimulation (middle panel; cLTP). Note that cLTP stimulation remarkably increased surface GluR1 immunostaining. The increase was completely blocked by APV (bottom panel; cLTP APV). Scale bar, 7 μm. (**B**) Quantitative analysis of surface GluR1 cluster density along dendrites. Data are expressed as percentages relative to the average of control neurons. In the absence of APV, cLTP stimulation significantly increased the density of surface GluR1 clusters (n = 21 cells; $p<0.01$, Scheffe's test). In contrast, in the presence of APV, no increase in surface GluR1 cluster density was observed following cLTP stimulation (cLTP APV). Error bars represent s.e.m.
doi:10.1371/journal.pone.0085367.g002

Localization of DA-actin and non-DA-actin is differentially regulated by glutamate receptor subtypes

We examined the effect of APV on DA-actin and total F-actin levels in dendritic spines. In the presence of 50 μM APV, drebrin and F-actin were localized at dendritic spines, and this localization was not changed by glutamate stimulation (photomicrographs in Fig. 6A).

However, quantitative analysis showed that the treatment of neurons with APV for 30 min resulted in significant increases in both drebrin and actin SDRs relative to controls. Interestingly, the increase in actin SDR (ca. 130% of control) is smaller than that of the drebrin SDR (ca. 180% of control; Fig. 6A). This indicates that NMDA receptor activity affects the basal accumulation level of DA-actin in dendritic spines more strongly than that of non-DA-actin. If non-DA-actin is not at all affected by APV, the above data suggest that about 40% of total F-actin is DA-actin. Furthermore, in the presence of APV, glutamate stimulation failed to decrease the drebrin SDR but did decrease the actin SDR (Fig. 6A). The disparity between drebrin and actin SDRs indicates that glutamate stimulation decreases the non-DA-actin even in the presence of APV.

Together, it is suggested that the NMDA receptor mediates both the glutamate-induced DA-actin exodus and the basal accumulation of DA-actin in dendritic spines, whereas glutamate receptor subtypes other than the NMDA receptor, such as AMPA or metabotropic glutamate receptors, mediate the non-DA-actin exodus.

The DA-actin exodus is not regulated by voltage-dependent Ca^{2+} channels or intracellular Ca^{2+} stores

Because NMDA receptor activation leads to Ca^{2+} influx, we examined whether Ca^{2+} regulates the DA-actin distribution. When extracellular Ca^{2+} was chelated by 20 mM ethylene glycol tetraacetic acid (EGTA), the localization pattern of drebrin and F-

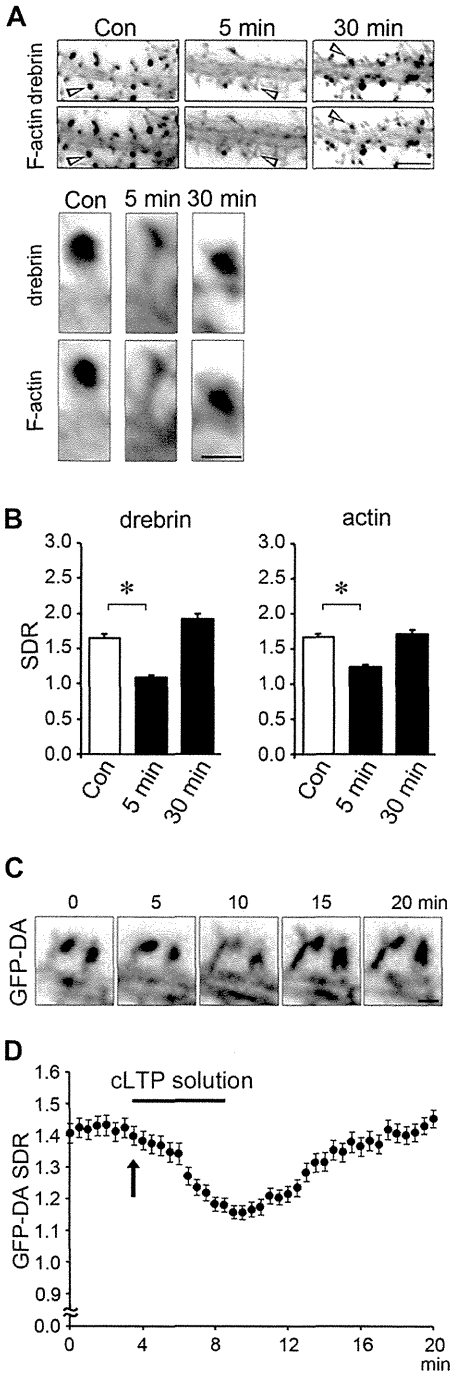

Figure 3. Chemical LTP (cLTP) stimulation induces the exodus and re-entry of DA-actin. (**A**) Neurons (21 DIV) were stimulated with a buffer containing 0 μM Mg^{2+}, 200 μM glycine, 20 μM bicuculline, 1 μM strychnine and 0.5 μM TTX (cLTP stimulation) for 3 min and then fixed 5 or 30 min after stimulation. The fixed cells were double-labeled for drebrin and F-actin. Scale bars, 5 μm and 1 μm in upper and lower panels, respectively. The lower panels show the higher-magnification images of the spines (indicated by arrow heads) in the upper panels. (**B**) Bar graphs represent the spine-dendrite ratios (SDRs) for drebrin and actin. cLTP stimulation significantly decreased the drebrin and actin SDRs at 5 min (n = 30 cells; $p<0.01$, Student's *t* test). Error bars represent s.e.m. (**C, D**) We transfected 7-DIV neurons with a GFP-drebrin A (GFP-DA)-expressing vector and performed time-lapse imaging at 21 DIV. Scale bar, 1 μm. (C) shows the GFP-DA images at 0, 5, 10, 15 and 20 min after the start of the time-lapse recording. The neurons were stimulated with cLTP solution from 3.5 min (indicated by an arrow) to 8.5 min. In (D), closed circles represent data obtained at 30-sec intervals. Error bars represent s.e.m. (n = 7 neurons). The GFP-DA SDR began to decrease soon after cLTP stimulation. When the stimulation was stopped, the GFP-DA SDR began to increase and recovered to control levels within 10 min.
doi:10.1371/journal.pone.0085367.g003

actin in dendritic spines was similar for both with and without glutamate stimulation (photomicrographs in Fig. 6B). However, quantitative analysis showed that EGTA treatment significantly increased both the drebrin and actin SDRs compared with control neurons. Following the extracellular Ca^{2+} chelation, glutamate stimulation failed to induce decreases in drebrin and actin SDRs (n = 30 cells; p = 0.88 for drebrin SDR, p = 0.84 for actin SDR; Student's *t* test; graphs in Fig. 6B). These data indicate that Ca^{2+} influx is involved in the changes in both DA-actin and non-DA-actin distribution.

Inhibition of L-type voltage-dependent Ca^{2+} channels with 20 μM nifedipine did not block glutamate-induced changes in drebrin and F-actin localization (photomicrographs in Fig. 6C). Quantitative analysis also showed that nifedipine treatment did not inhibit the glutamate-induced decreases in drebrin and actin SDRs. However, in the absence of glutamate stimulation, nifedipine treatment significantly increased the drebrin and actin SDR levels, similar to the results obtained with APV and EGTA treatments (graphs in Fig. 6C). This indicates that voltage-dependent Ca^{2+} channels regulate the accumulation of DA-actin in dendritic spines, but do not regulate the DA-actin exodus. However, we cannot exclude the possibility that the increase of the basal SDR is due to inhibition of voltage-dependent Ca^{2+} channels in the presynaptic terminus.

Inhibition of Ca^{2+} release from intracellular stores with 1 μM thapsigargin [32] did not block glutamate-induced changes in drebrin and F-actin localization (photomicrographs in Fig. 6D). Quantitative analysis showed that thapsigargin neither increased the drebrin and actin SDRs (n = 30 cells; p = 0.99 for drebrin SDR, p = 0.50 for actin SDR; Student's *t* test) nor blocked the glutamate-induced decreases in drebrin and actin SDRs (n = 30 cells: $p<0.01$, Scheffe's test; graphs in Fig. 6D).

Together, these data indicate that DA-actin exodus is regulated by NMDA receptors, but not by voltage-dependent Ca^{2+} channels. On the other hand, the basal accumulation of DA-actin in dendritic spines is regulated by both NMDA receptors and voltage-dependent Ca^{2+} channels. Ca^{2+} release from intracellular stores is not involved in either the DA-actin exodus or the basal accumulation of DA-actin.

Glutamate-induced DA-actin exodus is also dependent on myosin II ATPase activity

We examined whether myosin II ATPase is involved in the glutamate-induced DA-actin exodus. In the presence of aBL, drebrin localization at dendritic spines was not affected by glutamate stimulation (photomicrographs in Fig. 7), and glutamate stimulation did not induce a decrease in drebrin SDR (n = 30 cells; p = 0.06, Student's *t* test; graph in Fig. 7). Interestingly, the actin SDR was slightly, but significantly, decreased upon glutamate stimulation (graph in Fig. 7), although the decrease was not remarkable compared with that in the presence of iBL (Fig. 7). This result indicates that inhibition of myosin II ATPase does not completely block the exodus of F-actin, indicating that a small amount of F-actin other than DA-actin exits dendritic spines in response to glutamate stimulation.

Together, it is indicated that the glutamate-induced as well as the cLTP-induced DA-actin exodus depends on myosin II ATPase, but the glutamate-induced non-DA-actin exodus is at

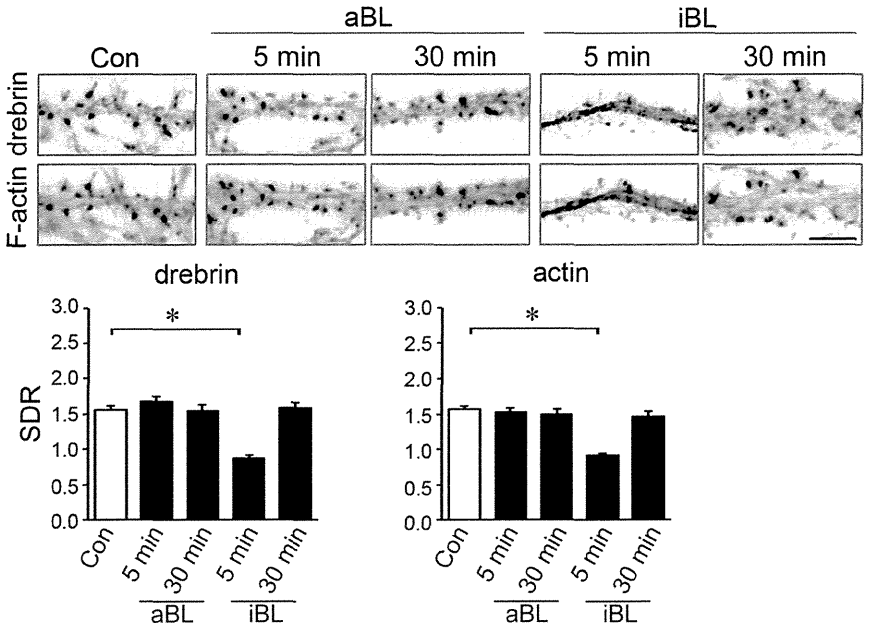

Figure 4. cLTP-induced DA-actin exodus is blocked by an inhibitor of myosin II ATPase. Neurons (21 DIV) were preincubated with 100 μM (S)-(−)-blebbistatin (aBL, the active form of blebbistatin) for 30 min and then stimulated with cLTP solution for 3 min. (R)-(+)-blebbistatin (iBL, the inactive form of blebbistatin) was used as a control. Scale bars, 5 μm. F-actin images indicate that spines kept their structure during the experiment although their shapes were changed. The aBL-treated neurons did not show a decrease in the drebrin and actin SDRs at either 5 min or 30 min after cLTP stimulation (n = 30 cells; Student's test), whereas iBL-treated neurons showed a significant decrease in the drebrin and actin SDRs at 5 min (n = 30 cells; $p<0.01$, Scheffe's test), similar to that observed in control neurons in Fig. 3. Error bars represent s.e.m.
doi:10.1371/journal.pone.0085367.g004

least partly independent of myosin II ATPase. This myosin II-independent loss of non-DA-actin might correspond to the NMDA receptor-independent loss of non-DA-actin shown in Fig. 6A.

The DA-actin exodus is not dependent on phosphorylation of myosin light chain

To examine whether the phosphorylation of myosin light chain (MLC) is involved in the DA-actin exodus, we inhibited myosin

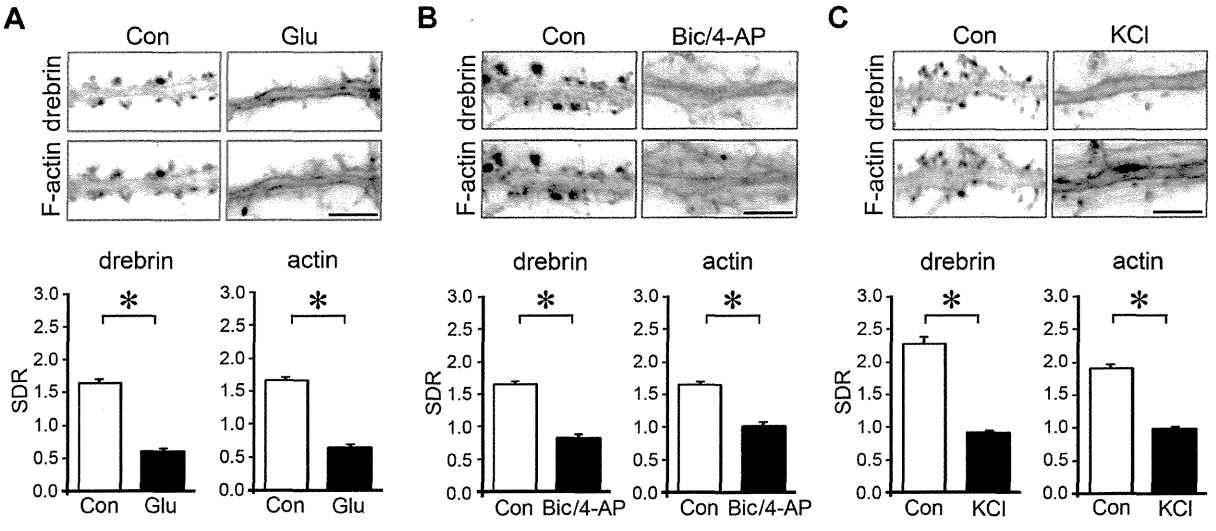

Figure 5. Effects of various excitatory stimulations on DA-actin distribution. Images were obtained from neurons (21 DIV) double-labeled for drebrin and F-actin. Bar graphs represent the spine-dendrite ratios (SDRs) for drebrin and actin. (**A–C**) Neurons were stimulated with 100 μM glutamate for 10 min (A), 50 μM bicuculline and 500 μM 4-aminopyridine (Bic/4-AP) for 10 min (B), or 90 mM KCl in Tyrode's solution for 5 min (C). F-actin images indicate that spines kept their structure during the experiment although their shapes were changed. After stimulation, the drebrin and F-actin clusters in the spines disappeared, and a linear staining pattern appeared along the dendrite. Both the drebrin and actin SDRs were significantly decreased (glutamate, n = 170 cells; Bic/4-AP, n = 30 cells; KCl, n = 30 cells; $p<0.01$, Student's *t* test). Note that the control drebrin and actin SDRs in (C) were greater than the other SDRs because Tyrode's solution was used instead of normal medium. Scale bars, 5 μm. Error bars represent s.e.m.
doi:10.1371/journal.pone.0085367.g005

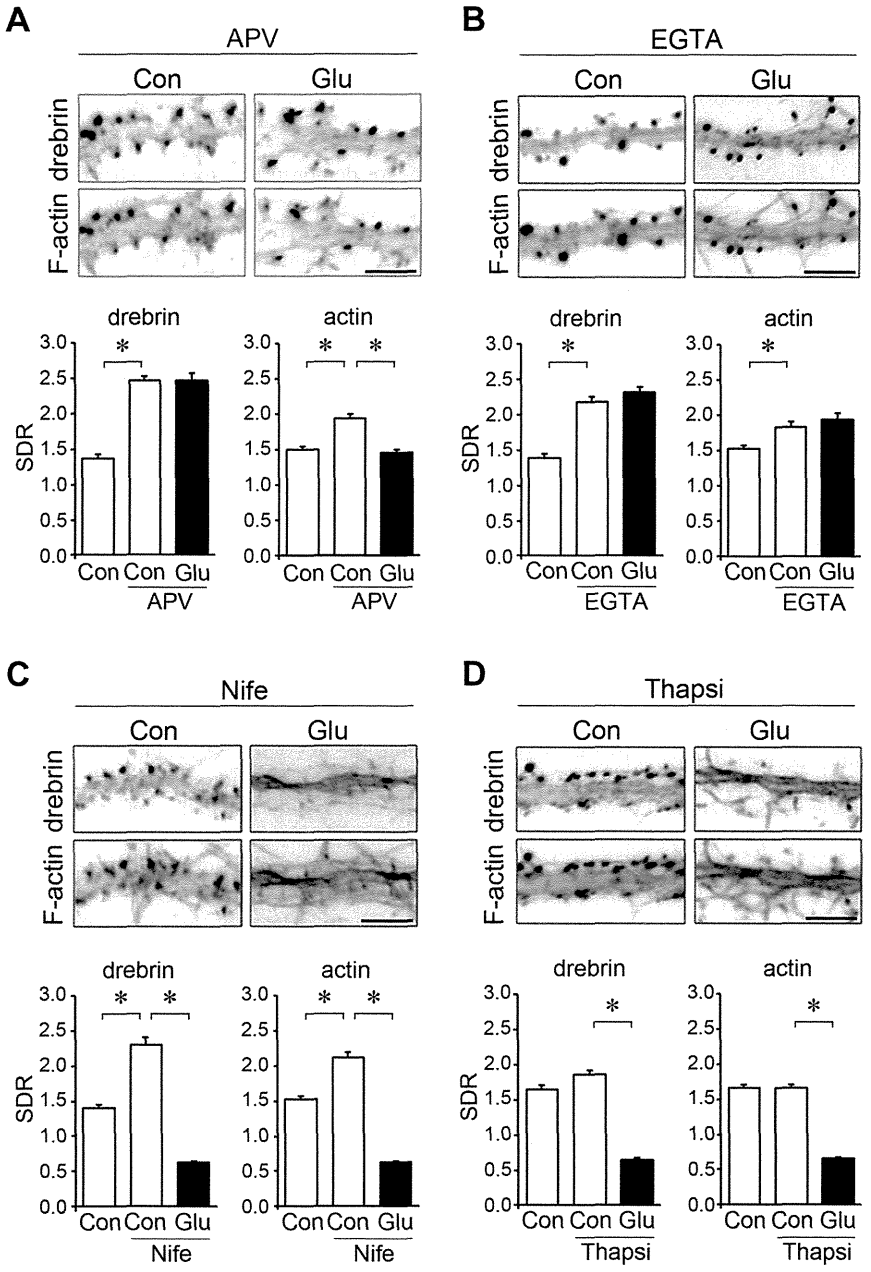

Figure 6. Effects of various inhibitors of Ca^{2+} entry on DA-actin distribution. Neurons (21 DIV) were incubated in normal medium containing 50 μM APV (A), 20 mM EGTA (B), 20 μM nifedipine (C), or 1 μM thapsigargin (D) for 30 min. The neurons were then stimulated with 100 μM glutamate for an additional 10 min. F-actin images indicate that spines kept their structure during the experiment although their shapes were changed. Scale bars, 5 μm. (**A**) APV pretreatment significantly increased both the drebrin and actin SDRs (n = 30 cells; $p<0.01$, Scheffe's test). In the presence of APV, glutamate stimulation significantly decreased the actin SDR (n = 30 cells; $p<0.01$, Student's *t* test) but not the drebrin SDR (n = 30 cells; $p = 0.52$, Student's *t* test). (**B**) EGTA significantly increased the drebrin and actin SDRs (n = 30 cells; $p<0.01$, Scheffe's test), and blocked the glutamate-induced decreases in drebrin and actin SDRs (n = 30 cells; Student's *t* test). (**C**) Nifedipine significantly increased the drebrin and actin SDRs (n = 30; $p<0.01$, Scheffe's test), but did not block the glutamate-induced decrease in drebrin and actin SDRs (n = 30; $p<0.01$, Scheffe's test). (**D**) Thapsigargin neither increased the drebrin and actin SDRs (n = 30; Student's *t* test) nor blocked the glutamate-induced decreases in drebrin and actin SDRs (n = 30; $p<0.01$, Scheffe's test). Error bars represent s.e.m.
doi:10.1371/journal.pone.0085367.g006

light chain kinase (MLCK). When MLCK activity was inhibited with 10 μM ML-7, glutamate stimulation induced the loss of drebrin and F-actin from dendritic spines (photomicrographs in Fig. 8A). Quantitative analysis showed that the ML-7 treatment did not change the drebrin and actin SDR levels compared with control neurons, and did not inhibit the glutamate-induced decreases in the drebrin and actin SDRs (Fig. 8A).

We then inhibited ROCK activity with 1 μM H-1152. In the presence of H-1152, glutamate stimulation induced the loss of drebrin and F-actin from dendritic spines (photomicrographs in Fig. 8B). Quantitative analysis showed that the H-1152 treatment did not change the drebrin and actin SDR levels compared with control neurons, and did not inhibit the glutamate-induced decreases in the drebrin and actin SDRs (Fig. 8B).